Combustion and Flame 162 (2015) 1422–1439

Contents lists available at ScienceDirect

Combustion and Flame

journal homepage: www.elsevier.com/locate/combustflame

Consumption speed and burning velocity in counter-gradient and gradient diffusion regimes of turbulent premixed combustion

Sina Kheirkhah *, Ömer L. Gülder

University of Toronto, Institute for Aerospace Studies, Toronto, Ontario M3H 5T6, Canada

ARTICLE INFO

Article history:
Received 4 May 2014
Received in revised form 6 November 2014
Accepted 7 November 2014
Available online 6 December 2014

Keywords:
V-shaped flame
Flame surface density
Consumption speed

ABSTRACT

Flame surface density, local consumption speed, and turbulent burning velocity of turbulent premixed V-shaped flames were investigated experimentally. A novel experimental apparatus was developed, which allows for producing relatively weak, moderate, and intense turbulence conditions. The experiments were performed for three turbulence intensities of about 0.02, 0.06, and 0.17, corresponding to weak, moderate, and intense turbulence conditions, respectively. For each turbulence condition, three mean bulk flow velocities of 4.0, 6.2, and 8.3 m/s, along with two fuel–air equivalence ratios of 0.6 and 0.7 were tested. The results show that intensifying the turbulence conditions significantly affects the flame front characteristics. Specifically, with increasing the turbulence intensity, the mean-progress-variable at which the flame surface density features a maximum decreases from values greater than 0.5 to values smaller than 0.5. This was argued to be linked to the switch of the tested experimental conditions from regime of counter-gradient to that of gradient diffusion. Spatially-averaged values of the local consumption speed and burning velocity were investigated in the present study. The results show that, for all experimental conditions tested, the local consumption speed varies between the unstretched laminar flame speed and 1.5 times the unstretched laminar flame speed. However, the spatially-averaged burning velocity is significantly dependent on the experimental conditions tested. Specifically, the result show that, for relatively intense turbulence conditions, the spatially-averaged turbulent burning velocity is proportional to the root-mean-square of the streamwise velocity.

1. Introduction

Turbulent premixed combustion is the operation mode of several engineering equipment, e.g., stationary gas turbines and spark ignition engines [1–3]. In these equipment, the combustion processes are associated with large values of turbulence intensities, i.e., ratio of the root-mean-square (RMS), u', to the mean of the reactants velocity, U, being close to 50% [4]. In order to investigate the characteristics of turbulent premixed flames at relatively large values of turbulence intensities, several experimental setups associated with Bunsen type, bluff-body stabilized, opposed jets, and swirl stabilized flames have been developed in the past, see for example the review papers by [5–7]. To the best knowledge of the authors, no experimental investigation has been performed to study characteristics of V-shaped flames at relatively large values of turbulence intensities. Specifically, the flame surface density (Σ), local consumption speed (S_{LC}), and turbulent burning velocity (S_T) of premixed V-shaped flames at large values of u'/U are yet to be investigated in detail. Investigations of the present study are performed using concepts pertaining to counter-gradient and gradient diffusion regimes of turbulent premixed combustion. Thus, the rest of the introduction is presented in two subsections. In the first subsection, a background pertaining to the counter-gradient and gradient diffusion regimes of turbulent premixed combustion is provided. In the second subsection, a summary of literature associated with flame surface density, local consumption speed, and turbulent burning velocity are presented.

1.1. Counter-gradient and gradient diffusion regimes of turbulent premixed combustion

Counter-gradient diffusion is referred to the turbulent transport of a scalar, e.g., the progress-variable (c), in a direction that c values increase [8]. Gradient diffusion, on the other hand, is associated with the turbulent transport of a scalar in a direction that it decreases. Several experimental investigations, e.g., Moss [9], Kalt et al. [10] and Frank et al. [11], and direct numerical simulation (DNS) studies, e.g., Veynante et al. [12] and Swaminathan et al. [13], have shown that both counter-gradient and gradient diffusion

* Corresponding author.

http://dx.doi.org/10.1016/j.combustflame.2014.11.009
0010-2180/

can occur in turbulent premixed flames. These studies [9–13] show that, for values of $u'/S_{L0} \lesssim 3$, where S_{L0} is the unstretched laminar flame speed, the flames feature counter-gradient diffusion. In order to study the occurrence of counter-gradient turbulent diffusion, past investigations estimated the turbulent flux of the progress-variable. For $u'/S_{L0} \lesssim 3$, Bray et al. [14] show that the turbulent flux of the progress-variable can be obtained from the following equation:

$$\widetilde{u''c''} \approx \tilde{c}(1-\tilde{c})(\overline{u_p} - \overline{u_r}), \tag{1}$$

where $\tilde{c}$ is the Favre-averaged value of c, that is, $\tilde{c} = \overline{\rho c}/\bar{\rho}$, with ρ being the density. In Eq. (1), c'' and u'' are the fluctuations of the progress-variable and velocity with respect to their corresponding Favre-averaged values, that is, $c'' = c - \tilde{c}$ and $u'' = u - \tilde{u}$. In Eq. (1), $\overline{u_p}$ and $\overline{u_r}$ are the mean velocity in the products and the reactants regions, respectively. Since Favre-averaged progress-variable ($\tilde{c}$) varies between zero and unity, $\tilde{c}(1-\tilde{c})$ varies between zero and 0.25. Also, heat release leads to gas acceleration across the flame front; and, as a result, $\overline{u_p}$ is greater than $\overline{u_r}$. According to Eq. (1), the above argument suggests that the turbulent flux of the progress-variable is always positive for $u'/S_{L0} \lesssim 3$. The sign of the turbulent flux of the progress-variable being positive means that the turbulent transport occurs from the reactants towards the products, which is opposite to the heat flux direction. Thus, the corresponding regime of turbulent combustion is referred to as the counter-gradient diffusion regime.

For $u'/S_{L0} \gtrsim 3$, studies of [10–12] show that, on an averaged basis, the turbulent transport of the progress-variable can be reversed from the products towards the reactants region. This means that $\widetilde{u''c''}$ becomes negative, with $u'' = \tilde{u} - u$. Veynante et al. [12] proposed that, for the entire range of values of u'/S_{L0} investigated, the Favre-averaged turbulent flux of the progress-variable can be estimated from the following equation:

$$\widetilde{u''c''} \approx \tilde{c}(1-\tilde{c})(\tau S_{L0} - 2\alpha u'), \tag{2}$$

where $\tau = \rho_r/\rho_p - 1$, with ρ_r and ρ_p being the reactants and products densities, respectively. In Eq. (2), α is a modification factor, with further details discussed in Section 3.2. It can be shown that the sign of the turbulent flux; and, as a result, occurrence of either counter-gradient or gradient diffusion regimes depend on:

$$N_B = \frac{\tau S_{L0}}{2\alpha u'}. \tag{3}$$

N_B is referred to as the Bray number in the literature. Eqs. (2) and (3) suggest that, for $N_B \gtrsim 1$, the Favre-averaged turbulent flux of the progress-variable is positive, resulting in counter-gradient diffusion. Conversely, for $N_B \lesssim 1$, the turbulent flux is negative, leading to gradient diffusion.

The formulation proposed by Veynante et al. [12], see Eq. (2), has been developed for planar turbulent premixed flames. Thus, application of Eq. (2) for estimation of the turbulent flux in non-planar turbulent premixed flames has been a matter of debate in the literature, see for example [15]. Pfadler et al. [15] experimentally estimated the turbulent flux of the progress-variable associated with a swirl stabilized turbulent premixed flame. Their results show that the model proposed in Eq. (2) underestimates the turbulent flux of the progress-variable in non-planar turbulent premixed flames. Nevertheless, the present study does not aim at estimating the turbulent flux of the progress-variable. In this study, only the Bray number (Eq. (3)), has been utilized for identifying the occurrence of either counter-gradient or gradient diffusion regimes.

1.2. Flame surface density, local consumption speed, and turbulent burning velocity

Flame surface density is defined as the averaged area of the flame surfaces per unit volume [6], given by the following equation:

$$\Sigma = \lim_{\Delta x \to 0} \frac{\Delta S}{(\Delta x)^3}, \tag{4}$$

where ΔS is the time-averaged area of the flame surfaces enclosed in a cube with a volume of $(\Delta x)^3$. Estimation of the flame surface density by means of Eq. (4) requires use of three-dimensional imaging techniques. To the best knowledge of the authors, no experimental investigation has estimated the flame surface density using Eq. (4) in V-shaped flame configuration. However, the flame surface density has been experimentally estimated using two-dimensional imaging techniques, see for example [16,17]. Shepherd [16] suggests that the flame surface density can be estimated from the following equation:

$$\Sigma = \frac{L}{A}, \tag{5}$$

where A is the area of the region enclosed between two mean-progress-variable ($\bar{c}$) contours. L is the averaged lengths of the flame front contours positioned inside the region with the area A. Since Eq. (5) is developed based on two-dimensional imaging technique, the estimated value of the flame surface density can potentially differentiate from the counter-part obtained from Eq. (4). For Bunsen-type flames, Bell et al. [18] performed a DNS study and estimated the flame surface density using two-dimensional contours and three-dimensional flame surfaces. Their results show that the flame surface density estimated based on two-dimensional contours is 25–33% smaller than that estimated based on the three-dimensionally resolved flame surfaces.

Variation of the flame surface density across the flame region has been investigated in several past studies pertaining to V-shaped flames; see for example, [16,17,19–21]. Results of past studies [16,17,19–21] show that variation of Σ with $\bar{c}$ features a parabolic-like distribution, that is skewed towards a mean-progress-variable greater than 0.5. Arguments provided in Shepherd [16] show that the flame fronts are composed of structures, referred to as cusps, that are mainly formed on the products side of the flame region. Skewness of the flame surface density profiles towards $\bar{c} \gtrsim 0.5$ is attributed to the cusp formation [16].

In turbulent premixed V-shaped flames, the local consumption speed has been mainly estimated [16,17,22–24] using the following formulation:

$$S_{LC} = S_{L0} I_0 \int_{-\infty}^{+\infty} \Sigma \, d\eta, \tag{6}$$

where S_{L0} is the unstretched laminar flame speed. In Eq. (6), I_0 is the ratio of the laminar flame speed to the unstretched laminar flame speed, and is referred to as the stretch factor. The stretch factor can be obtained from the following equation [6]:

$$I_0 = \frac{S_L}{S_{L0}} = 1 - \mathcal{L}\kappa, \tag{7}$$

where S_L, $\mathcal{L}$, and κ are the laminar flame speed, Markstein length, and the flame front curvature, respectively. The Markstein length depends on the fuel–air mixture [25]. Specifically, it is shown that, for fuel–air mixtures with unity Lewis number, the Markstein length is negligible [6]. As a result, the stretch factor is unity [6]. Methane–air mixtures, with fuel–air equivalence ratios close to 0.7, feature unity stretch factor [6,25,26]. The values of the stretch factor for fuel–air mixtures with a non-unity Lewis number have

been experimentally estimated and can be found in [25–27]. In Eq. (6), η is the coordinate system perpendicular to the mean-progress-variable contours. Since the flame surface density is negligible for small and large values of η, Eq. (6) can be simplified to the following equation:

$$S_{LC} \approx S_{L0} I_0 \int_{\eta_1}^{\eta_2} \Sigma \, d\eta, \tag{8}$$

where η_1 and η_2 are the lower and upper bounds of integration, respectively. Past studies associated with V-shaped flame configuration [17,20,21] show that increasing the turbulence intensity increases the spread of the flame surfaces in a larger region. This means that $\eta_2 - \eta_1$ increases with increasing the turbulence intensity. On the other hand, past studies associated with V-shaped flame configuration [17,20,21] show that increasing the turbulence intensity decreases the flame surface density. Thus, the trend associated with effect of turbulence intensity on the local consumption speed is not known a priori for V-shaped flames. Results of Tang and Chan [21] show that, Σ and the bounds of integration vary such that the integral in Eq. (8); and, as a result, the local consumption speed increases with increasing the turbulence intensity.

In comparison to relatively large number of investigations associated with estimation of the local consumption speed in turbulent premixed V-shaped flames, studies pertaining to evaluating the turbulent burning velocity is scarce in the literature [6]. For a given height above the flame-holder, Guo et al. [17] estimated the turbulent burning velocity in V-shaped flame configuration using:

$$S_T = U \sin(\psi), \tag{9}$$

where U is the mean bulk flow velocity; and ψ is the angle between the tangent line to the contour of $\bar{c} = 0.5$ and the vertical axis. Results of Guo et al. [17] show that the turbulent burning velocity normalized by the RMS of the reactants velocity measured at the exit of the burner (S_T/u') features a power-law relation with the product of the Lewis number (Le) and the Karlovitz stretch factor (K), which is estimated using the following equation:

$$K = 0.157 \left(\frac{u'}{S_{L0}}\right)^2 Re_{\Lambda}^{-0.5}, \tag{10}$$

where $Re_{\Lambda} = u'\Lambda/\nu$, with Λ and ν being the integral length scale and the reactants kinematic viscosity, respectively. In Eq. (10), both u' and Λ are estimated for non-reacting flow condition. Results of Guo et al. [17] show that increasing KLe decreases S_T/u'. This means that, for a given value of u', increasing the flame rate of stretch decreases the normalized turbulent burning velocity, which is in agreement with the results associated with other flame geometries, see for example Bradley et al. [28].

The above arguments show that characteristics of turbulent premixed V-shaped flames are significantly dependent on the turbulence intensity. Although engineering applications of turbulent premixed combustion are associated with relatively large values of turbulence intensity, review of literature shows that past experimental investigations associated with V-shaped flames have been performed for relatively small and moderate values of turbulence intensities ($u'/U \lesssim 0.1$). This range of (u'/U) variation corresponds to $u'/S_{L0} \lesssim 3$ for hydrocarbon–air mixtures. In the present study, turbulent premixed combustion characteristics, specifically, flame surface density, local consumption speed, and turbulent burning velocity, for relatively large values of u'/U are studied. Large values of turbulence intensity are produced using a novel experimental setup. The setup allows for generating turbulence intensities up to 0.18, which corresponds to $u'/S_{L0} \lesssim 11$. The rest of the paper is organized as follows. First, the experimental methodology is presented. In the results section, turbulent flow characteristics for non-reacting flow condition are investigated. Then, flame surface density, local consumption speed, and turbulent burning velocity are discussed.

2. Experimental methodology

The burner setup utilized for producing the V-shaped flames, the coordinate system, the turbulence generating arrangements, the measurement techniques, and the experimental conditions tested are presented in this section.

2.1. Burner setup

The V-shaped flames were produced using the burner shown in Fig. 1(a). The burner is composed of an expansion section, a settling chamber, a contraction section, and a nozzle. The expansion section has an expansion area ratio of about four. Close to the entrance of the expansion section, a baffle disk is placed in order to disperse the entering air–fuel mixture and the seeding flow, see Fig. 1(a). A settling chamber, equipped with five square-mesh screens, is installed after the expansion section. The settling chamber is followed by a contraction section with a contraction area ratio of approximately seven. After the contraction section, a nozzle with inner diameter of 48.4 mm is placed. An enlarged view of the nozzle section is presented in Fig. 1(b) along with photograph of a representative turbulent premixed V-shaped flame. A flame-holder is placed close to the exit of the nozzle, see Figs. 1(a) and (b). The flame-holder is cylindrical in shape, and has a diameter (d) of 2 mm. A flame-holder support was used to fix the flame-holder, see Fig. 1(a). Distance between the flame-holder centerline and the exit plane of the burner was fixed at 4 mm for all the experimental conditions tested.

2.2. Coordinate system

The coordinate system utilized in the present investigation is Cartesian, as shown in Fig. 2. The origin of the coordinate system is located equidistant from both ends of the flame-holder, and 5 mm above the burner exit plane. The y-axis of the coordinate system is normal to the exit plane of the burner. The x-axis is normal to both y-axis and the flame-holder centerline. The z-axis is normal to both x and y axes and lies along the span of the flame-holder.

2.3. Turbulence generating arrangements

Three turbulence generating arrangements were utilized in the present study. For the first arrangement, turbulence was associated with the mesh screens in the settling chamber, see Fig. 1(a). For this arrangement, turbulence generating apparatus was not utilized. For this reason, the turbulence intensity associated with the first arrangement was relatively small. This will be discussed in further details in the following section. The experiments associated with the first arrangement were performed in order to provide a benchmark for comparison with relatively moderate and intense turbulence conditions. Details associated with the second and the third turbulence generating arrangements are provided below.

The technical drawing associated with the second turbulence generation arrangement is presented in Fig. 3(a). The generator shown in Fig. 3(a) is a stainless steel perforated plate, with outer diameter (D) of 48.4 mm and a thickness of 1 mm. The turbulence generator plate has sixty-seven circular holes, which are arranged in hexagonal pattern, see Fig. 3(a). Each hole has a diameter (D_h) of 3.9 mm. The distance between two neighboring holes (s) is 5.7 mm. This arrangement of holes results in a plate blockage ratio of approximately 58%.

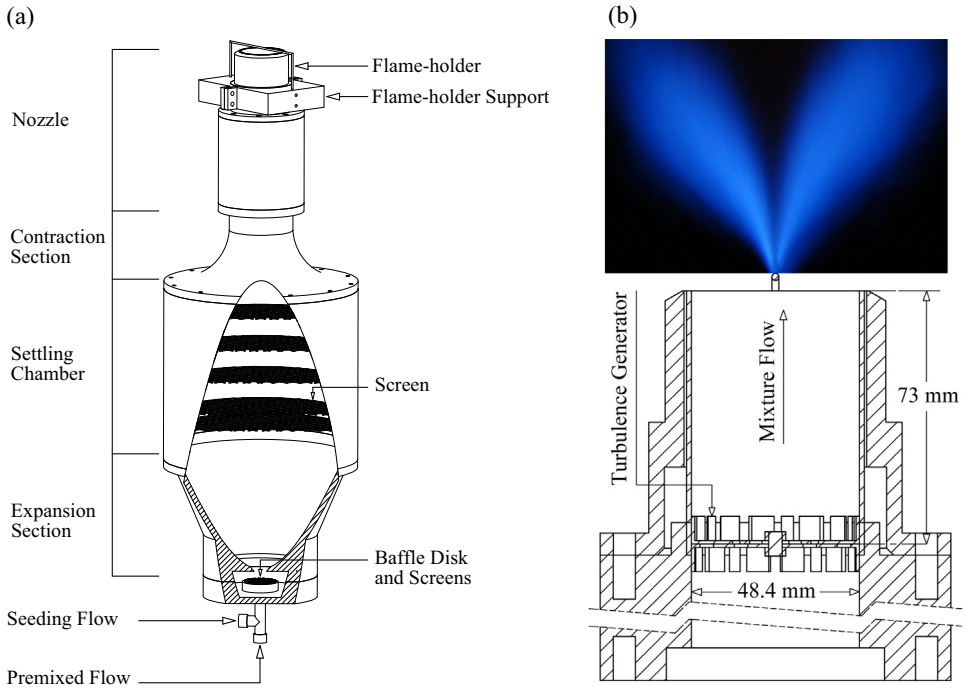

Fig. 1. (a) The burner setup and (b) the nozzle section of the burner along with a representative image of the combustion region.

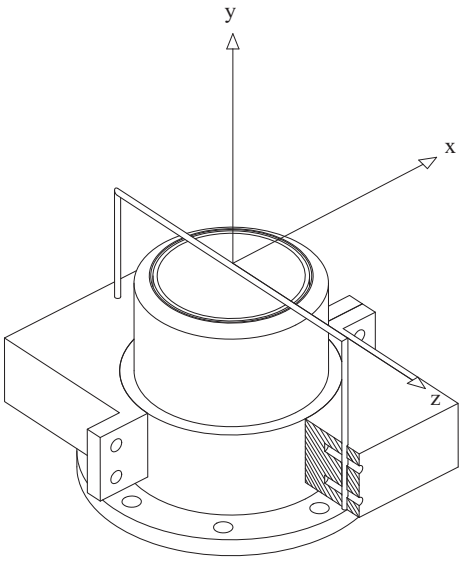

Fig. 2. Coordinate system.

Figure 3(b) represents the technical drawing of the third turbulence generation arrangement. The generator shown in Fig. 3(b) is composed of two perforated plates, with the plate technical drawing presented in Fig. 3(a). In Fig. 3(b), r and θ are the distance between two neighboring circular holes as well as the relative angular position of the plates, respectively. The results show that both r and θ significantly affect the turbulent flow characteristics. Using a trial and error technique, these parameters were tuned such that the turbulence intensity produced by the arrangement is maximized. The pertaining values of r and θ are approximately 15 mm and 60°, respectively.

Depending on the first, second, or third arrangement tested, either no generator was placed in the nozzle section, the generator shown in Fig. 3(a) was installed, or the generator shown in Fig. 3(b) was placed inside the nozzle section of the burner, respectively. The results show that, for distances between the turbulence generating mechanism and the exit plane of the nozzle smaller than about 50 mm, the flames occasionally flash back and stabilize on the turbulence generating mechanism rather than the flame-holder. In order to avoid this problem, for the second and the third arrangements, the turbulence generators were placed one and a half nozzle diameters, i.e., about 73 mm, upstream of the nozzle exit, see Fig. 1(b).

2.4. Measurement techniques

The Mie scattering and the Particle Image Velocimetry (PIV) techniques were utilized in the experiments. The former was used to obtain the flame front; and the latter was used to estimate the velocity field characteristics for non-reacting flow conditions. For both techniques, the olive oil droplets were utilized for seeding purposes. Details associated with the Mie scattering and PIV techniques are provided below.

Mie scattering is elastic scattering of light, with wavelength λ, from particles with average size d_p, when $d_p \gtrsim \lambda$ [29]. In the application of the Mie scattering technique for studying premixed flames, it is assumed that combustion occurs inside a relatively thin layer. This assumption is referred to as the flamelet assumption [30]. This implies that if the reactants are seeded with particles which evaporate at the flame front, the light intensities scattered from the particles significantly change across the flame front. This abrupt change in the light intensities was used for obtaining the flame front in the present study.

For relatively small and moderate values of turbulence intensity ($u'/U \lesssim 0.1$), which corresponds to $u'/S_{L0} \lesssim 3$, it has been previously established that the Mie scattering technique can be utilized for obtaining the turbulent premixed flame characteristics, see for example [31–34]. Also, for relatively large values of turbulence intensity (u'/U up to 0.3 and u'/S_{L0} up to 9), the Mie scattering technique has been utilized for obtaining the flame front characteristics in past investigations associated with turbulent premixed

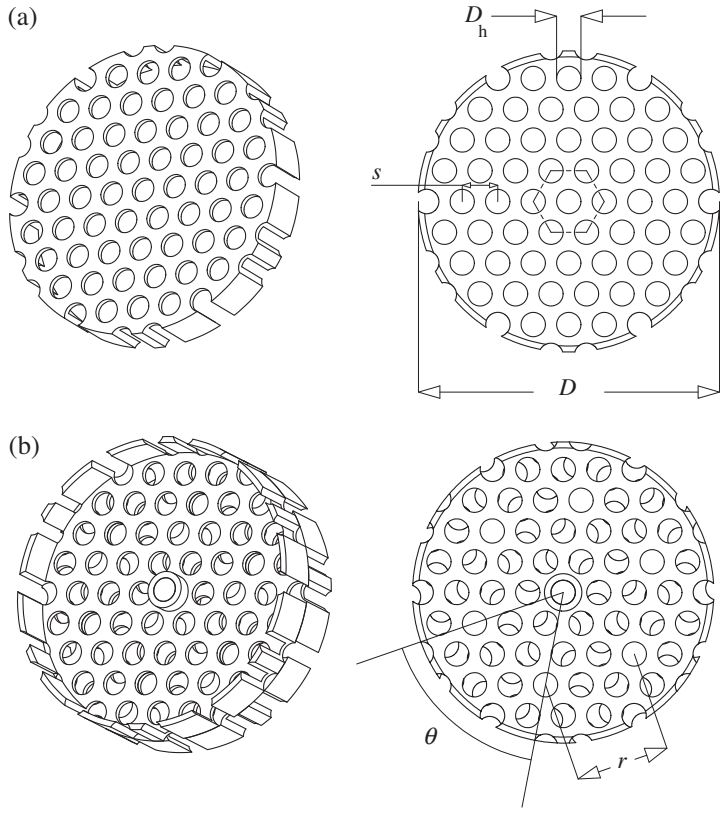

Fig. 3. (a) and (b) turbulence generating mechanisms utilized for the second and the third arrangements, respectively.

combustion, see for example Filatyev et al. [35] and Lachaux et al. [36]. Thus, it is expected that the Mie scattering can be potentially utilized for obtaining flame front characteristics for relatively intense turbulence conditions of the present study, similar to those tested in [35,36].

The hardware associated with the Mie scattering technique consists of a CCD camera and a Nd:YAG pulsed laser, with the details provided in [32]. All the experiments were performed at the plane of $z/d = 0$. For each experimental condition tested, 1000 images were acquired. The recorded images were binarized and filtered using the algorithm detailed in Kheirkhah and Gülder [32].

The Particle Image Velocimetry (PIV) was performed in order to estimate the non-reacting flow characteristics. The hardware associated with the PIV is identical to that used for the Mie scattering experiments. For each experimental condition tested, 1000 PIV image pairs were acquired. The interrogation box size was set to 16 pixels, with zero overlap between the boxes. The separation time between the laser pulses, was selected such that the average distance traced by the seeding particles in each interrogation box was approximately 25% of the size of the interrogation box. This measure was taken to avoid particles loss between consecutive images.

2.5. Experimental conditions

The tested experimental conditions are tabulated in Table 1. Methane grade 2, i.e., methane with 99% chemical purity, was used as the fuel in the experiments. In the table, Flames A–F, G–L, and M–R correspond to the first, the second, and the third turbulence generating arrangements, respectively. All velocity statistics presented in Table 1 were estimated using the PIV technique for non-reacting flow condition and without the flame-holder in place. Mean and RMS streamwise velocity profiles were averaged along the x-axis (from $x/d = -12$ to 12) at $z/d = 0$ and $y/d = 1$. In Table 1, U and u'_0/U correspond to the averaged values; and are referred to as the mean bulk flow velocity and the turbulence intensity, respectively. A detailed description of the non-reacting flow field is provided in Section 3.1. For each turbulence generating arrangement, three mean bulk flow velocities of $U = 4.0$, 6.3, and 8.3 m/s were tested. For each mean bulk flow velocity, two fuel–air equivalence ratios of $\phi = 0.6$ and 0.7 were examined. The unstretched laminar flame speed (S_{L0}) was extracted from [37]. The laminar flame thickness was estimated from: $\delta_L = \mathcal{D}/S_{L0}$, where $\mathcal{D} = \nu/(PrLe)$. The Lewis number (Le), the Prandtl number (Pr), and the kinematic viscosity (ν) are estimated for the reactants at standard temperature and pressure conditions; and are approximately unity, 0.71, and 1.57×10^{-5} m^2/s, respectively. Σ_{max} and a pertain to the characteristics of the flame surface density and will be defined later in the discussions associated with Eq. (17).

The integral length scale (Λ) was estimated using the following equation:

$$\Lambda(x,y) = \int_0^{h^*} R_{uu}(x,y,h)\mathrm{d}h, \tag{11}$$

where h^* is the vertical extent at which the autocorrelation of the streamwise velocity (R_{uu}) first attains zero value. The autocorrelation is obtained from:

$$R_{uu}(x,y,h) = \frac{\overline{[u(x,y) - \overline{u(x,y)}][u(x,y+h) - \overline{u(x,y+h)}]}}{\overline{\left[u(x,y) - \overline{u(x,y)}\right]^2}}, \tag{12}$$

where the over-bar symbol in Eq. (12) represents ensemble averaging over time.

In both Eqs. (11) and (12), x and y are the horizontal and vertical positions of the point at which the integral length scale is

Table 1
Tested experimental conditions.

	U[a]	ϕ	S_{L0}[a]	δ_L[b]	u'_0/U	u'_0/S_{L0}	Λ_0[b]	$\overline{\overline{\Lambda}}$[b]	$\overline{\overline{\Lambda'}}$[b]	Re_{Λ_0}	Da	K	Σ_{max}[c]	a
Flame A	4.0	0.6	0.13	0.17	0.02	0.6	2.6	8.8	6.8	14.1	17.6	0.02	2.1	1.3
Flame B	4.0	0.7	0.20	0.11	0.02	0.4	2.6	8.8	6.8	14.1	34.3	0.01	1.6	1.4
Flame C	6.2	0.6	0.13	0.17	0.02	0.8	2.5	8.1	5.2	18.9	12.0	0.03	2.8	1.3
Flame D	6.2	0.7	0.20	0.11	0.02	0.6	2.5	8.1	5.2	18.9	23.5	0.01	2.4	1.4
Flame E	8.3	0.6	0.13	0.17	0.02	1.5	2.4	8.0	4.1	31.9	6.2	0.07	2.0	1.2
Flame F	8.3	0.7	0.20	0.11	0.02	1.0	2.4	8.0	4.1	31.9	12.5	0.03	2.2	1.3
Flame G	4.0	0.6	0.13	0.17	0.06	1.7	4.2	4.6	4.0	61.6	10.2	0.06	0.6	1.1
Flame H	4.0	0.7	0.20	0.11	0.06	1.1	4.2	4.6	4.0	61.6	19.9	0.02	0.4	1.0
Flame I	6.2	0.6	0.13	0.17	0.06	2.7	3.8	4.2	3.7	88.7	5.8	0.12	0.6	1.1
Flame J	6.2	0.7	0.20	0.11	0.06	1.8	3.8	4.2	3.7	88.7	11.4	0.05	0.5	1.0
Flame K	8.3	0.6	0.13	0.17	0.06	3.7	3.8	4.3	3.6	121.6	4.2	0.20	0.7	1.1
Flame L	8.3	0.7	0.20	0.11	0.06	2.4	3.8	4.3	3.6	121.6	8.3	0.08	0.6	1.1
Flame M	4.0	0.6	0.13	0.17	0.18	5.5	6.3	6.3	5.2	298.2	4.7	0.28	0.3	0.6
Flame N	4.0	0.7	0.20	0.11	0.18	3.6	6.3	6.3	5.2	298.2	9.3	0.12	0.3	0.6
Flame O	6.2	0.6	0.13	0.17	0.17	8.2	5.5	6.1	6.5	449.4	3.1	0.51	0.4	0.6
Flame P	6.2	0.7	0.20	0.11	0.17	5.4	5.5	6.1	6.5	449.4	6.2	0.22	0.3	0.5
Flame Q	8.3	0.6	0.13	0.17	0.17	11.0	5.5	6.2	4.4	524.3	2.1	0.85	0.4	0.6
Flame R	8.3	0.7	0.20	0.11	0.17	7.2	5.5	6.2	4.4	524.3	3.8	0.36	0.4	0.5

[a] The unit is m/s.
[b] The unit is mm.
[c] The unit is 1/mm.

evaluated, respectively. Thus, Eq. (11) allows for obtaining a two-dimensional array for the integral length scale. Note that, there exists a maximum for y in Eqs. (11) and (12). Our analysis shows that, for $y/D \gtrsim 0.8$, the streamwise velocity autocorrelation does not attain a zero value. In other words, for $y/D \gtrsim 0.8, h^*$ does not exist. As a result, estimation of the integral length scale in the vertical extent was limited to the points with vertical positions smaller than $0.8D$. In Table 1, three integral length scale values are provided: $\Lambda_0, \overline{\overline{\Lambda}}$, and $\overline{\overline{\Lambda'}}$. The integral length scale estimated close to the exit of the burner, i.e., $x/d = 0$ and $y/d = -1$, is represented by Λ_0. In other words,

$$\Lambda_0 = \Lambda(0, -2). \tag{13}$$

$\overline{\overline{\Lambda}}$ and $\overline{\overline{\Lambda'}}$ are the integral length scales associated with non-reacting flow without the flame-holder and with the flame-holder, respectively. Both $\overline{\overline{\Lambda}}$ and $\overline{\overline{\Lambda'}}$ are spatially-averaged values and are estimated from the following equation:

$$\overline{\overline{\Lambda}},\ \overline{\overline{\Lambda'}} = \int_0^{0.8D} \int_{-0.4D}^{0.4D} \Lambda^* \, dx \, dy. \tag{14}$$

The limits of integration in Eq. (14) is selected in order to avoid effect of jet shear layers in the estimations. This is further discussed in Section 3.1.

In Table 1, Reynolds and Damköhler numbers are calculated from $Re_{\Lambda_0} = u'_0 \Lambda_0 / \nu$ and $Da = S_{L0} \Lambda_0 / (u'_0 \delta_L)$, respectively. In the table, K is the Karlovitz stretch factor and is estimated using Eq. (10). For the estimation of the Karlovitz stretch factor, values of u'_0 were used as the RMS velocity fluctuations and $\Lambda = \Lambda_0$. Abdel-Gayed et al. [38] show that Eq. (10) can be obtained from the definition of the Karlovitz number, i.e., $Ka = (\delta_L/\eta_K)^2$ [1], where η_K is the Kolmogorov length scale. In the derivation provided in Abdel-Gayed et al. [38], it is assumed that the turbulence is isotropic and the $Re_{\Lambda_0} \gtrsim 60$. Although these two conditions are not entirely satisfied for the experimental conditions tested in the present study, the Karlovitz stretch factor was utilized in the discussions. This is because the formulation presented in Eq. (10) allows for the collapse of the experimental results. Further details are provided in Section 3.2.

All the tested experimental conditions are overlaid on the turbulent premixed combustion diagram, presented in Fig. 4. The results in Fig. 4 show that the experimental conditions associated with the first, the second, and the third turbulence generation arrangements mainly correspond to the wrinkled flames, the corrugated flames, and the thin reaction zones, respectively. As shown in Fig. 4, the data symbols associated with the first, the second, and the third turbulence generating arrangements pertain to the turbulence intensities of $u'_0/U \approx 0.02, u'_0/U \approx 0.06$, and $u'_0/U \approx 0.17$, respectively. For the results presented in Fig. 4 as well as the results to be presented in the following section, the data symbols associated with the reacting flow conditions are color-coded. Specifically, the results pertaining to the first (Flames A–F), second (Flames G–L), and third (Flames M–R) turbulence generating mechanisms are denoted by the blue,[1] red, and black colors, respectively.

3. Results and discussion

The results are grouped into two subsections. In the first subsection, characteristics of the non-reacting flow are studied. Then, in the second subsection, characteristics of the flame brush thickness, the flame surface density, the local consumption speed, and the turbulent burning velocity are investigated.

3.1. Non-reacting flow analysis

The results are grouped into two subsections: characteristics of the background flow field and characteristics of the flow field with the flame-holder.

3.1.1. Characteristics of the background flow field

Details associated with the mean and RMS of the velocity field along with the integral length scale pertaining to the streamwise velocity are studied. Figures 5(a)–(c), (d)–(f), and (g)–(i) present variations of the mean streamwise velocity, RMS of the streamwise velocity, and RMS of the transverse velocity, respectively. The results are normalized by the mean bulk flow velocity of the corresponding experiment. The solid, dashed, and dotted-dashed lines pertain to mean bulk flow velocities of 4.0, 6.2, and 8.3 m/s respec-

[1] For interpretation of color in Fig. 4, the reader is referred to the web version of this article.

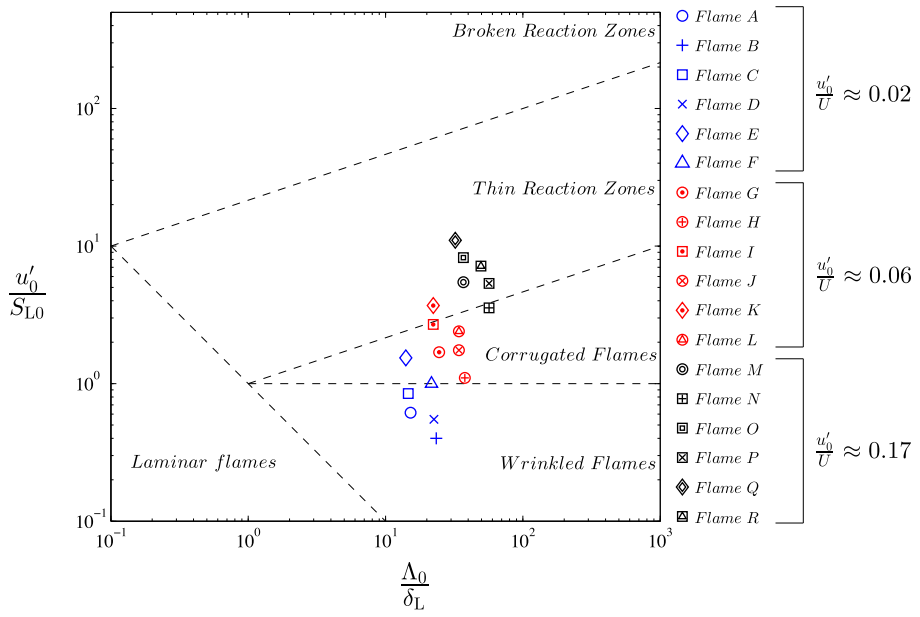

Fig. 4. The experimental conditions overlaid on the Borghi diagram [1]. Data symbols associated with $u'_0/U \approx 0.02$, 0.06, and 0.17 correspond to the first, the second, and the third turbulence generating mechanisms, respectively.

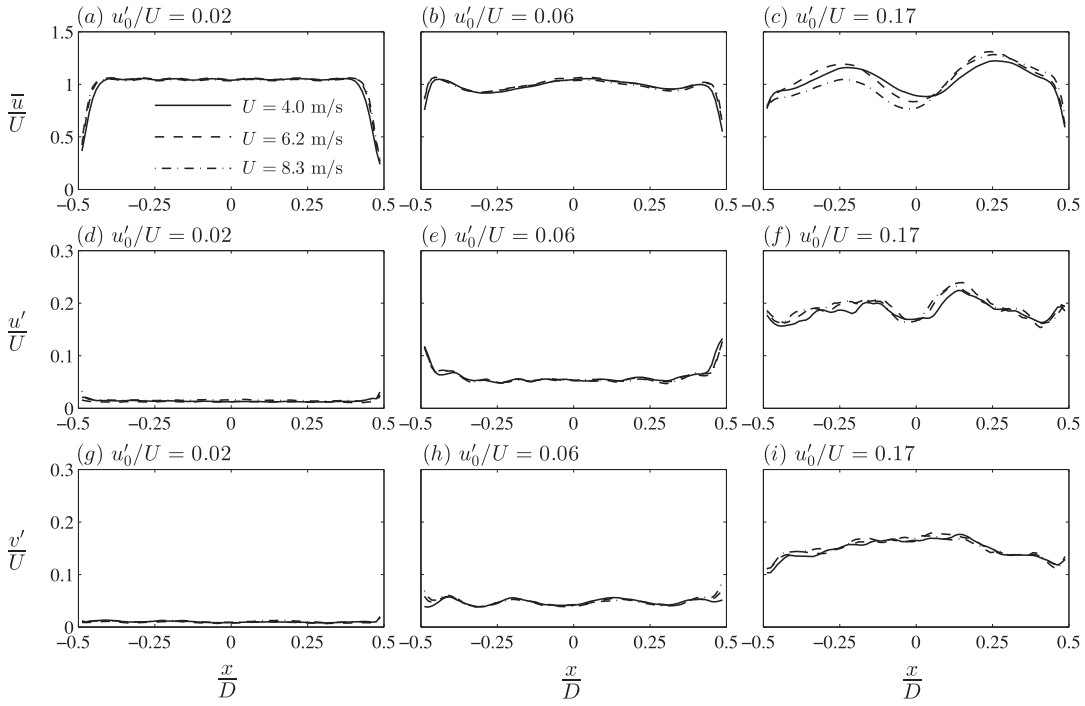

Fig. 5. Velocity statistics estimated for non-reacting flow condition and at $y/d = 1$. (a)–(c), (d)–(f), and (g)–(i) correspond to mean streamwise, RMS streamwise, and RMS transverse velocities, respectively. The first, the second, and the third columns are associated with the first, the second, and the third turbulence generating mechanisms, respectively.

tively. In Fig. 5, the velocity statistics are measured at $y/d = 1$. The first, second, and third columns correspond to the first, second, and third turbulence generating mechanisms, respectively. As shown in Fig. 5, variations of $\bar{u}/U, u'/U$, and v'/U across the transverse direction are independent of the mean bulk flow velocities tested and collapse. For relatively small value of turbulence intensity, the velocity statistics are homogeneous close to $x/D = 0$ (see the first column in Fig. 5). However, for relatively moderate and large values of turbulence intensity, the statistics of the velocity field become inhomogeneous. This is similar to the results reported in past investigations, see for example [39–41], and is a characteristic of perforated plate turbulence generators.

Variation of the RMS of the streamwise velocity along the jet centerline (y-axis) is presented in Fig. 6. Results in Figs. 6(a), (b), and (c) pertain to the first, the second, and the third turbulence generating mechanisms, respectively. The solid, dashed, and dotted-dashed lines correspond to mean bulk flow velocities of 4.0, 6.2, and 8.3 m/s, respectively. The results in Figs. 6(b) and (c) show that the normalized RMS of the streamwise velocity decays along the centerline. Results of past studies [41–46] show that decrease

and/or increase of RMS of the streamwise velocity depends on the turbulence generating mechanism utilized for producing the turbulent flow. For perforated plates and active grids, similar to the results presented in Figs. 6(b) and (c), those presented in [41–43] show that the normalized RMS of the streamwise velocity decreases with downstream distance. However, for fractal-type turbulence generators as well as combination of several perforated plates, results of past investigations show that the normalized RMS of the streamwise velocity first increases and then decreases with downstream distance, see for example [44–46].

Figure 6(a) shows that, for relatively small vertical distances ($y/D \lesssim 0.5$) and for the first turbulence generating arrangement, u'/U is almost constant. However, for normalized vertical distances greater than about 0.5, increasing y/D increases u'/U. The flow physics associated with the first turbulence generating mechanism is similar to that of the developing region of a turbulent round jet, see for example [47–50]. Specifically, results presented in [47–50] show that the turbulence intensity increases along the centerline of the developing round jets. Bogusławski and Popiel [47] argue that the reason for the increasing trend is due to diffusion of the turbulent kinetic energy from the shear layers towards the centerline of the jet. The shear layer development is associated with the roll up phenomenon [49]. This characteristic is illustrated by representative Mie scattering images in Fig. 7. Figures 7(a), (b), and (c) correspond to mean bulk flow velocities of $U = 4.0, 6.2,$ and 8.3 m/s, respectively. The directions of the roll ups are shown by the arrows in the figures. As can be seen from the figures, the size of vortices participating in the roll up process is significantly larger for $U = 4.0$ m/s in comparison to those associated with $U = 6.2$ and 8.3 m/s. This is speculated to cause large velocity fluctuations for the condition pertaining to $U = 4.0$ m/s in comparison to those associated with $U = 6.2$ and 8.3 m/s. Thus, it is expected that the RMS of the stramwise velocity to increase with y/D. Also, it is expected that this increase to be more pronounced for $U = 4.0$ m/s in comparison to $U = 6.2$ and 8.3 m/s.

Variations of the integral length scale (Λ) pertaining to the first, the second, and the third turbulence generating mechanisms are presented in Figs. 8(a), (b), and (c), respectively. The results are shown for mean bulk flow velocity of $U = 4.0$ m/s. Analysis of the results (not presented here) show that the integral length scale significantly increases close to $x/D = \pm 0.5$. This is due the shear layers and has been reported in past studies, see for example Daniele et al. [51]. The significant increase of the integral length scale smears out the variation of Λ in the domain of investigation. For this reason, the horizontal extent of the domain of data presentation is selected to be smaller than the burner diameter, i.e., $0.8D$. The vertical extent of the domain of data presentation is smaller than those presented in Figs. 6 and 7. This is because, for $y/D \gtrsim 0.8$, the autocorrelation of the streamwise velocity data (R_{uu}) does not cross the vertical axis; and, as a result, the integral length scale cannot be estimated. This was discussed in Section 2 in detail.

Figure 8(a) shows that, for relatively small values of y/D, the integral length scale is relatively small. However, at large vertical distances, Λ significantly increases. The increase of the integral length scale along the vertical axis is a characteristic of developing turbulent round jets, see for example Antonia et al. [52]. In comparison to results associated with the first turbulence generating mechanism, those pertaining to the second and third turbulence generating mechanisms show that the spatial variation of Λ is negligible in the domain of investigation. The value of Λ averaged over the domain of investigation is denoted by $\overline{\overline{\Lambda}}$ and is presented in Table 1 for all experimental conditions tested. The values of $\overline{\overline{\Lambda}}$ are similar to the perforated plates hole diameter and spacing between the holes.

In essence, the results presented in Figs. 6–8 indicate that the flow physics pertaining to the second and the third turbulence generating mechanisms are similar to decaying turbulence of a grid. However, for the first turbulence generating mechanism, the flow physics is dominated by characteristics of developing region of turbulent round jets. This was demonstrated by the increase of the turbulence intensity and integral length scale along the vertical axis.

3.1.2. Characteristics of flow over the flame-holder

Variation of the mean streamwise velocity, RMS of the streamvise velocity, and RMS of the transverse velocity are presented in Figs. 9(a), (b), and (c), respectively. The results in the figures are presented for mean bulk flow velocity of $U = 4.0$ m/s and $y/d = 1$. In the figures, the solid, dashed, and dotted-dashed lines correspond to the first, the second, and the third turbulence generating mechanisms, respectively. Comparison of the results in Fig. 9 with those in Fig. 5 shows that the flame-holder strongly influences the turbulent flow field. The results in Fig. 9(a) show that close $x/D = 0$ the mean velocity significantly decreases. This decrease is a result of the flame-holder wake and is a characteristic of flow over circular cylinders [53]. The RMS of the streamwise and transverse velocities feature relatively large values close to the vertical axis ($x/D = 0$) as shown in Figs. 9(b) and (c). As argued in [53], appearance of the peaks is due to the roll up of shear layers on both sides of the flame-holder, which leads to the vortex shedding phenomenon. In order to investigate this, instantaneous vorticiy contours for

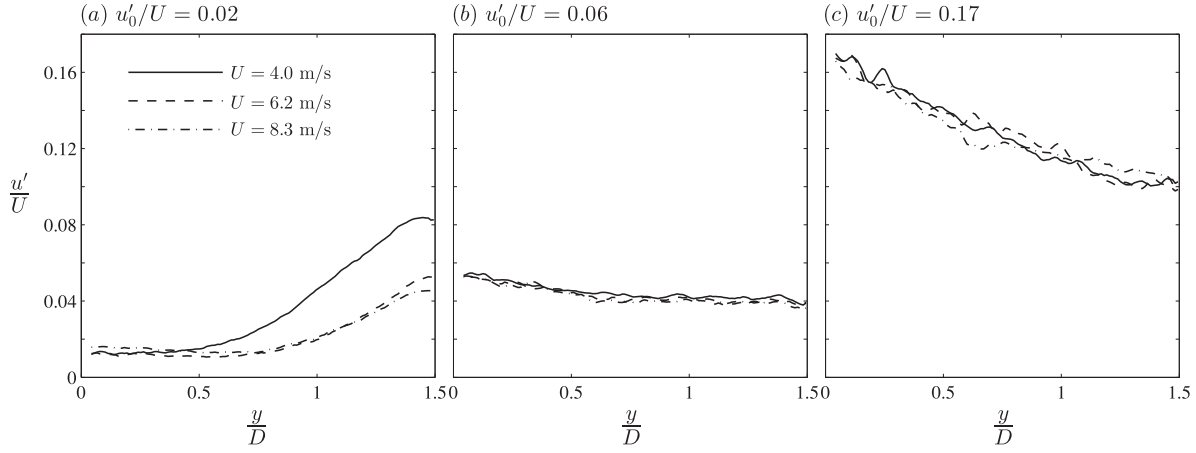

Fig. 6. Variation of the normalized RMS streamwise velocity along the jet centerline. (a), (b), and (c) Pertain to the first, the second, and the third turbulence generating arrangements, respectively.

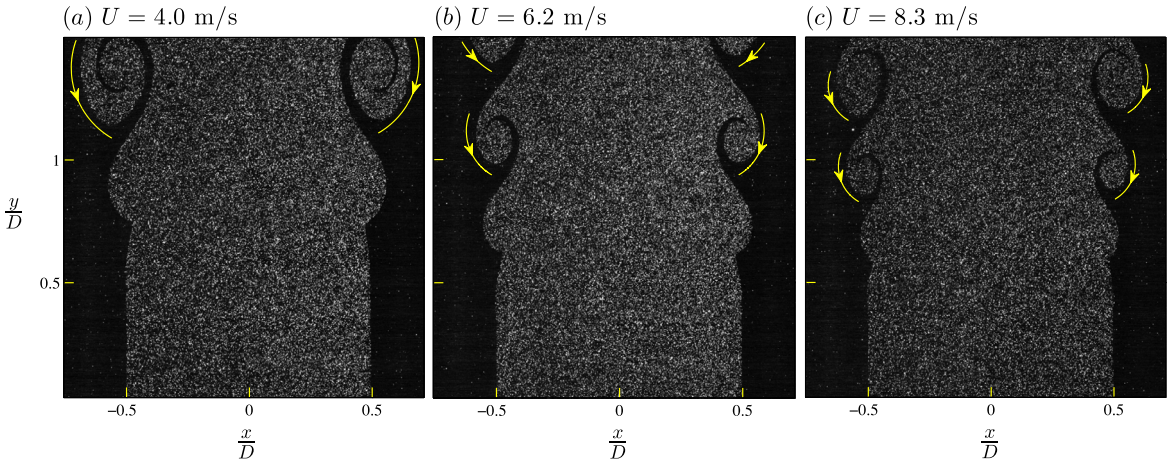

Fig. 7. Representative Mie scattering images demonstrating the shear layers roll up phenomenon. The results are associated with the first turbulence generating mechanism. (a), (b), and (c) correspond to mean bulk flow velocities of $U = 4.0$, 6.2, and 8.3 m/s, respectively.

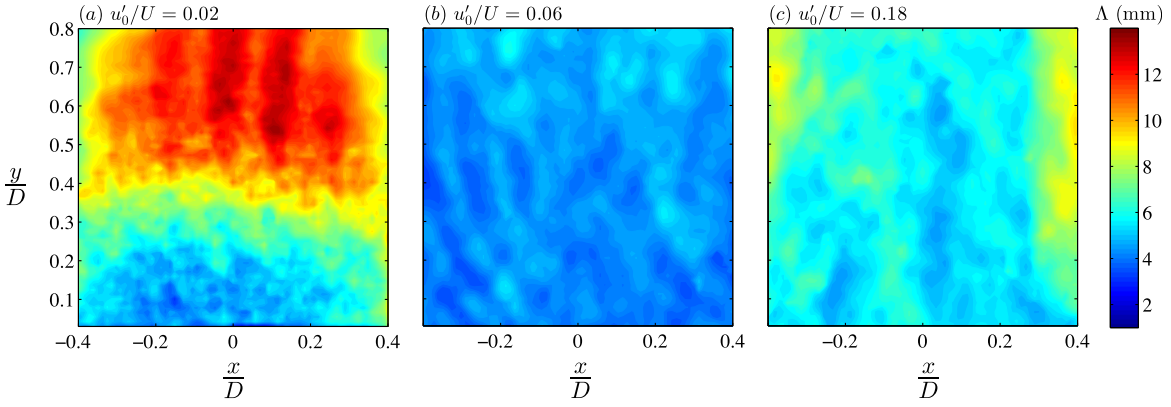

Fig. 8. The integral length scale. The results are associated with $U = 4.0$ m/s. (a), (b), and (c) correspond to the first, the second, and the third turbulence generating mechanisms, respectively.

$U = 4.0$ m/s are presented in Fig. 10. The results in Figs. 10(a), (b), and (c) correspond to relatively small, moderate, and large values of turbulence intensity, respectively. The results in the figure show that, relatively close to the flame-holder, the vorticity values are significantly large on both sides of the flame-holder. This causes the large values of the RMS streamwise and transverse velocities close to the flame-holder. The results in Figs. 10(a) and (b) show that, the vortex shedding phenomenon exists for the conditions associated with the first and the second turbulence generating arrangements. However, Fig. 10(c) shows that, for relatively large values of turbulence intensity, the vortex shedding phenomenon cease to occur. This is due to the relatively strong turbulence background produced by the third turbulence generating mechanism.

Variation of the integral length scale associated with the first, the second, and the third turbulence generating mechanisms are presented in Figs. 11(a), (b), and (c), respectively. The results are shown for mean bulk flow velocity of $U = 4.0$ m/s. Comparison of the results presented in Figs. 11(a)–(c) with those presented in Figs. 8(a)–(c) show that, the flame-holder causes reduction of the integral length scale in a region close to the vertical axis. In order

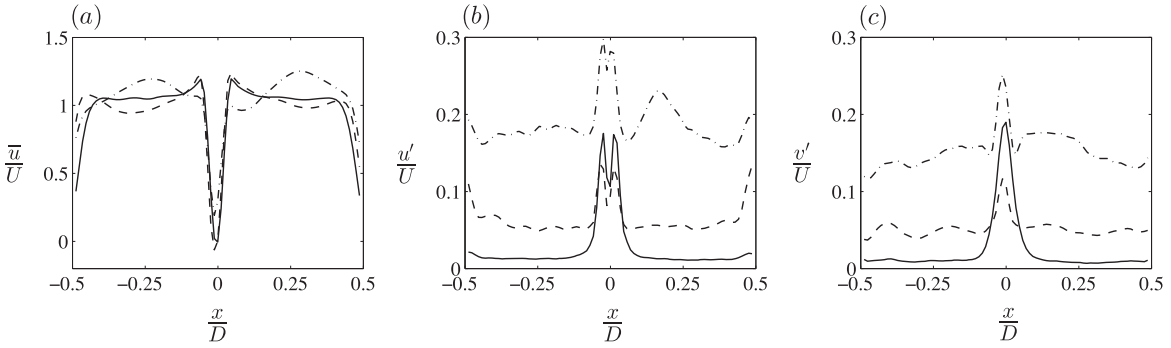

Fig. 9. Statistics of the velocity data. The results pertain to $U = 4.0$ m/s and $y/d = 1$. (a), (b), and (c) pertain to mean streamwise velocity, RMS streamwise velocity, and RMS transverse velocity, respectively. The solid, dashed, and dotted-dashed lines pertain to the first, the second, and the third turbulence generating mechanisms, respectively.

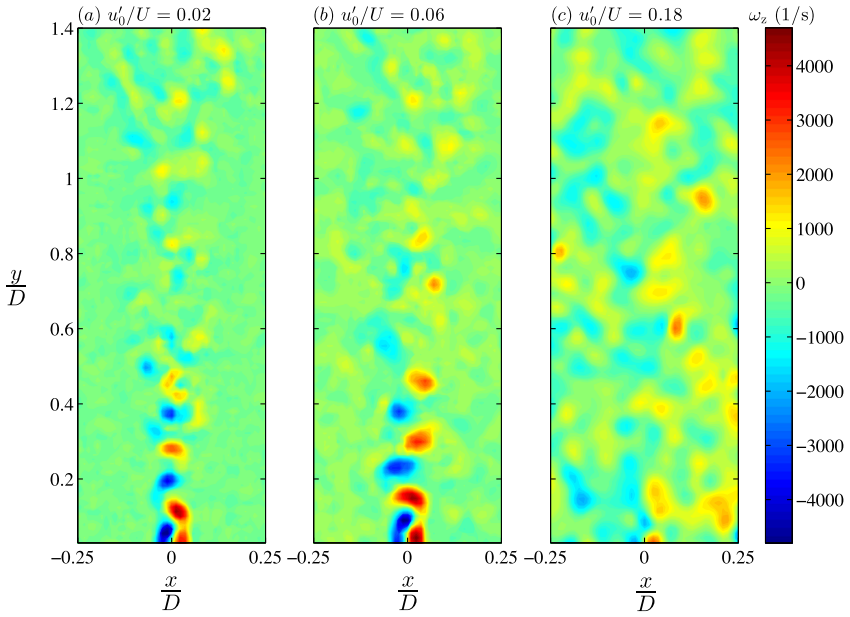

Fig. 10. Representative contours of instantaneous vorticity. The results are associated with $U = 4.0$ m/s. (a), (b), and (c) correspond to the first, the second, and the third turbulence generating mechanisms, respectively.

to investigate this, the autocorrelation of the streamwise velocity data (R_{uu}) associated with two representative points, one located inside the region with small values of Λ and one positioned outside the region are presented. Specifically, values of R_{uu} pertaining to points $P_1, P_2; P_3, P_4$; and P_5, P_6 are presented in Figs. 11(d), (e), and (f), respectively. The results in Figs. 11(d) and (e) show that R_{uu} associated with the points inside the region pertaining to small values of integral length scale feature oscillations along the vertical axis. However, R_{uu} associated with those outside of the region pertaining to small values of Λ do not feature oscillations. This is due to the vortex shedding phenomenon. Occurrence of vortex shedding for relatively small and moderate values of turbulence intensity was previously shown in Figs. 10(a) and (b). Since the vortical structures shown in Figs. 10(a) and (b) are positioned in a relatively ordered manner in the vertical direction, the velocity data become significantly correlated at certain positions close to y/D-axis resulting in the oscillation shown in Figs. 11(d) and (e). In comparison to the results presented in Figs. 11(d) and (e), those presented in Fig. 11(f) show that R_{uu} does not feature oscillations along the vertical axis. This is due to the mitigation of vortex shedding previously discussed in the results associated with Fig. 10(c). The mitigation of vortex shedding results in the non-oscillatory decay of the autocorrelation of the streamwise velocity data along y/D. Integral length scale averaged over the domain shown in Fig. 11 is referred to as $\overline{\overline{\Lambda'}}$ and is presented in Table 1.

RMS of the velocity fluctuations along with the integral length scale associated with the autocorrelation of the streamwise velocity data have been utilized in past studies pertaining to V-shaped flames in order to quantify the effect of turbulence on flame dynamics, see for example [16,17,19,32–34]. In these studies, the turbulent flow characteristics pertain to the background flow and are measured close to the exit of the corresponding burners. Analysis of the results presented in this section shows that both the RMS of the streamwise velocity as well as the integral length scale can vary in the domain of investigation. However, our analyses show that presentation of the reacting flow results based on turbulence characteristics averaged over the domain of investigation do not significantly change the trends and conclusions. For this reason and in order to be consistent with the results of past V-shaped flame investigations, e.g., [16,17,19,32–34], the background turbulent flow characteristics measured close to the exit of the burner were utilized in the analyses presented in the next section.

In the present study, the RMS of the steamwise velocity and the integral length scale associated with the streamwise velocity were not estimated for the reacting flow conditions. For a Bunsen-type flame and for methane–air mixtures, results presented in Pfadler et al. [54] show that the RMS of the reactants velocity and the integral length scale are about 10% and 50% larger in the products region compared to the reactants region, respectively. Our analyses show that these variations do not affect the trends associated with the results of the reacting flow condition.

3.2. Reacting flow analysis

The Mie scattering images show that the flame front topology is significantly affected by the turbulence intensity (u'_0/U). In order to demonstrate the effect of u'_0/U on the flame front topology, three representative Mie scattering images associated with experimental conditions of Flames E, K, and Q are presented in Figs. 12(a), (b), and (c), respectively. Note that, for the results presented in Fig. 12, the mean bulk flow velocity and the fuel–air equivalence ratio are fixed at $U = 8.3$ m/s and $\phi = 0.6$, respectively. The turbulence intensities pertaining to the results presented in Figs. 12(a), (b), and (c) are $u'_0/U = 0.02$, 0.06, and 0.17, respectively. For the results presented in Fig. 12, the flame fronts are highlighted by the contours overlaid on the Mie scattering images. The flame fronts associated with the images in Fig. 12 were obtained using the flame front detecting algorithm detailed in Kheirkhah and Gülder [32]. As shown in the figure, increasing the turbulence intensity enhances the flame front wrinkling. As discussed in Veynante et al. [12], gradient diffusion occurs for significantly wrinkled turbulent premixed flames. Thus, it is expected that increasing u'_0/U changes the regime of turbulent flames from counter-gradient to gradient diffusion. Since flame front characteristics such as the flame brush thickness (δ_t), flame surface density (Σ), local consumption speed (S_{LC}), and turbulent burning velocity (S_T) are linked to the topology of the flame surfaces, it is argued that the turbulence intensity significantly affects characteristics of the flames investigated. The rest of the results are grouped into three subsections, addressing details associated with the flame

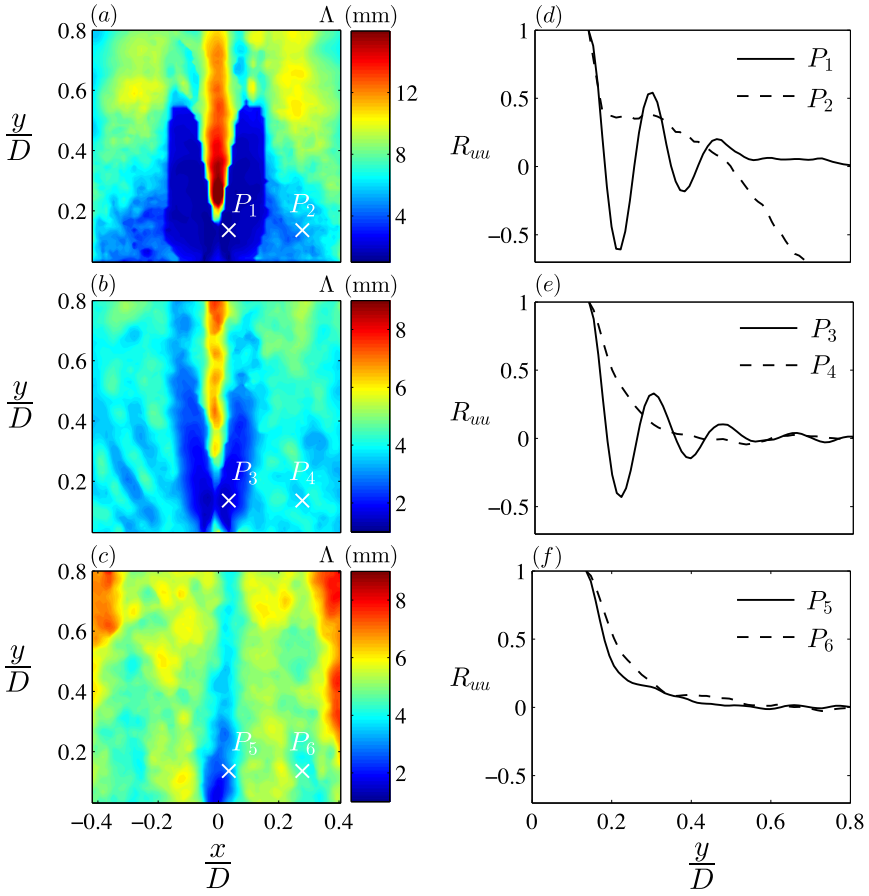

Fig. 11. (a), (b), and (c) are the integral length scales associated with the first, the second, and the third turbulence generating mechanisms, respectively. (d), (e), and (f) correspond to streamwise velocity autocorrelation pertaining to the results shown in (a), (b), and (c), respectively. The results are presented for $U = 4.0$ m/s.

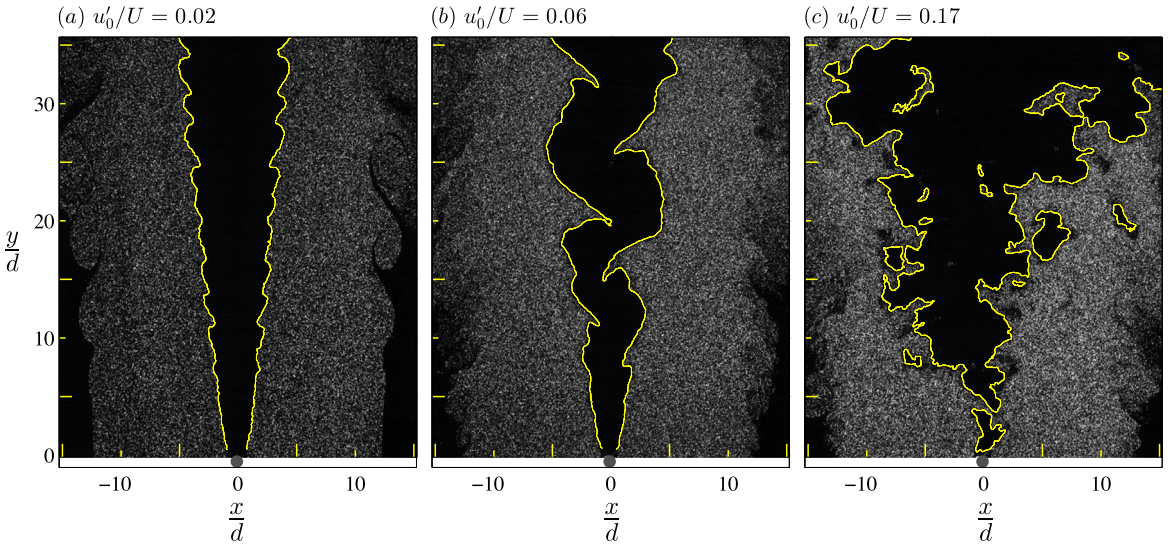

Fig. 12. Representative Mie scattering images. (a), (b), and (c) correspond to experimental conditions of Flames E, K, and Q, respectively.

brush thickness, flame surface density, as well as the local consumption speed and the turbulent burning velocity.

3.2.1. Flame brush thickness

Analysis of the flame brush thickness is of significant importance in studying turbulent flames. This is partly due to the contribution of the flame brush thickness in estimation of the local consumption speed. For all experimental conditions tested, the Mie scattering images were divided into two regions: $x/d \geqslant 0$ and $x/d < 0$. The flame fronts associated with $x/d \geqslant 0$ and $x/d < 0$ are referred to as the right and left wings of the flame front, respectively. For both right and left wings of the flame fronts, the flame brush thickness was estimated using the following equation:

$$\delta_t = \frac{1}{\max(|d\bar{c}/dx|)}. \tag{15}$$

For each experimental condition tested, $\bar{c}$ was estimated by averaging the corresponding binarized Mie scattering images. Variation of the flame brush thickness along the vertical axis is presented in Fig. 13. Kheirkhah and Gülder [34] investigated underlying physics associated with the flame brush thickness for the experimental conditions of the present study. Figure 13 is reproduced from [34]. In each sub-figure, the data points on the right and left hand sides refer to right and left wings of the flame front, respectively. Also, the results in each sub-figure are presented for fixed mean bulk flow velocity and turbulence intensity along with two fuel–air equivalence ratios of $\phi = 0.6$ and 0.7. Figures 13(a)–(c), (d)–(f), and (g)–(i) correspond to turbulence intensities of about 0.02, 0.06, and 0.17, respectively. The results show that, at a fixed vertical distance from the flame-holder, the flame brush thickness is significantly dependent on the turbulence intensity. Specifically, increasing u_0'/U increases δ_t. For example, at $\phi = 0.6, U = 8.3$ m/s, and $y = 20$ mm (see Flame E, K, and Q conditions), increasing turbulence intensity from 0.02 to 0.06, and 0.17 increases the flame brush thickness from about 0.5 to 1.5, and 5 mm, respectively. This is due to enhanced wrinkling and spread of the flame surfaces, with the representative images presented in Fig. 12. The increasing trend of δ_t with u_0'/U is in agreement with previous studies, see for example [17,55].

The results in Fig. 13 show that effect of the fuel–air equivalence ratio on the flame brush thickness is dependent on the turbulence intensities tested. Specifically, for relatively moderate values of turbulence intensity, increasing the fuel–air equivalence ratio increases the flame brush thickness. This is a characteristic of turbulent premixed V-shaped flames and has been previously investigated in the studies of Kheirkhah and Gülder [32–34], Namazian et al. [55], and Guo et al. [17]. In comparison to the relatively moderate value of turbulence intensity, the results in Figs. 13(a)–(c) and (g)–(i) show that the flame brush thickness is not sensitive to the fuel–air equivalence ratio.

3.2.2. Flame surface density

The flame surface density (Σ) was obtained using Eq. (5). In order to estimate L and A in the equation, the domain of investigation was divided into 19 sectors. The sectors were bounded between two contours of mean-progress-variables: $\bar{c} + \Delta\bar{c}/2$ and $\bar{c} - \Delta\bar{c}/2$. The width of the mean-progress-variable intervals, i.e., $\Delta\bar{c}$, was selected to be 0.05. This interval width provides proper resolution for the flame surface density variation and avoids scatter in the data. Values of L, A, and Σ are presented in Figs. 14(a), (b), and (c), respectively. Note that the values of the flame surface density at $\bar{c} = 0$ and 1 were set to zero in Fig. 14(c). The results are presented for fixed values of mean bulk flow velocity ($U = 8.3$ m/s) and fuel–air equivalence ratio ($\phi = 0.6$). Also, the results are shown for relatively small, moderate, and large values of turbulence intensities, pertaining to the first, the second, and the third turbulence generating mechanisms, respectively. For relatively moderate values of turbulence intensity, variations of L and A with the mean-progress-variable ($\bar{c}$) are similar to the results presented in Shepherd [16] and Tang and Chan [21]. The results in Figs. 14(a) and (b) show that increasing the turbulence intensity increases both L and A. Results presented in Fig. 12 showed that increasing the turbulence intensity increases the length of the flame fronts. This is in agreement with the results presented in Fig. 14(a). Also the results in Figs. 12 and 13 showed that intensifying the turbulence conditions enhances the spread of the flame surfaces in the domain of investigation and increases the flame brush thickness. These are in agreement with the results presented in Fig. 14(b). Although increasing the turbulence intensity increases both L and A, the flame surface density decreases with increasing u_0'/U as shown in

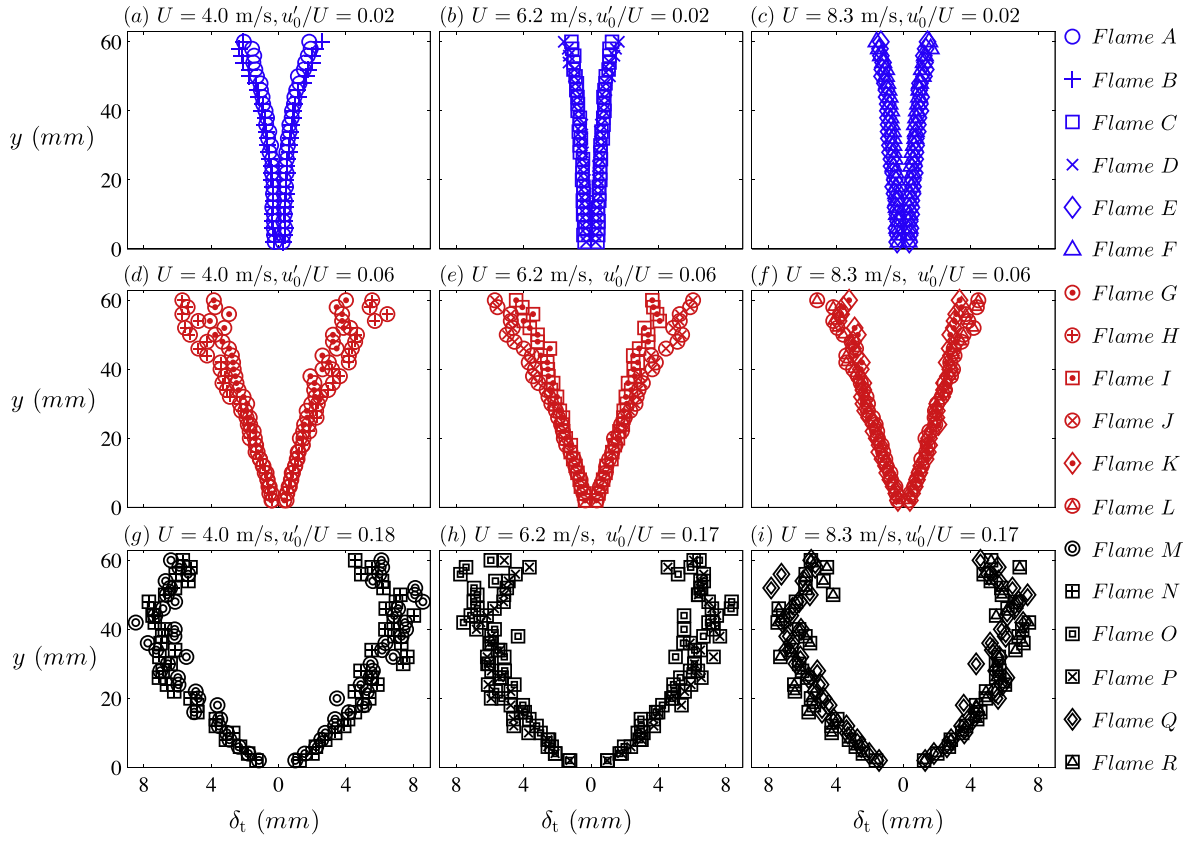

Fig. 13. Variation of the flame brush thickness with the vertical distance from the flame-holder. (a)–(c), (d)–(f), and (g)–(i) correspond to relatively small ($u_0'/U \approx 0.02$), moderate ($u_0'/U \approx 0.06$), and large ($u_0'/U \approx 0.17$) values of the turbulence intensity, respectively. The results are reproduced from Kheirkhah and Gülder [34].

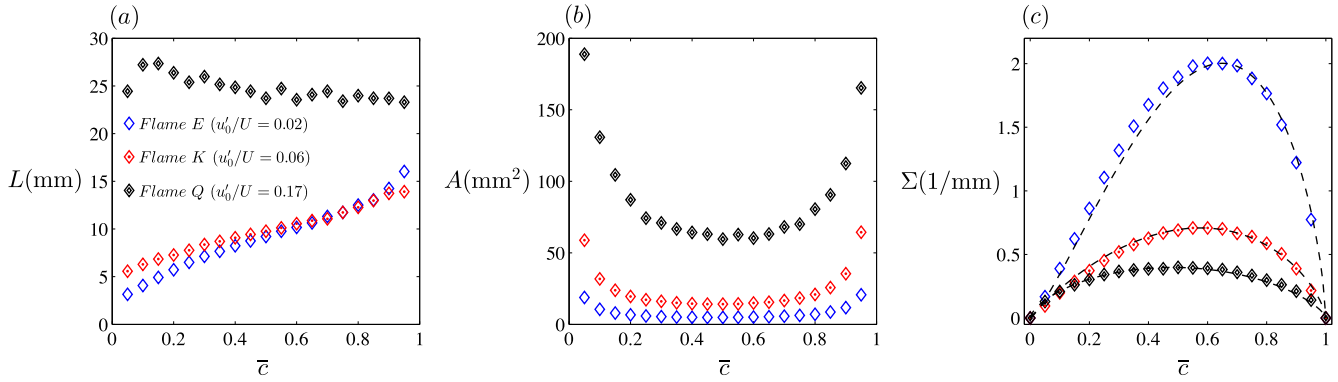

Fig. 14. (a), (b), and (c) correspond to the averaged flame front length, the area, and the flame surface density profiles, respectively. The results pertain to $\phi = 0.6$ and $U = 8.3$ m/s. The dashed lines in (c) are the fits obtained from the model proposed in Eq. (17).

Fig. 14(c). This is in agreement with the results presented in Tang and Chan [21] and Lam et al. [20]. Note that, the decrease of the flame surface density with increasing u'_0/U does not necessarily result in decrease of the local consumption speed. This is discussed in further detail in the following subsection.

The results show that the mean-progress-variable at which the flame surface density maximizes, referred to as $\bar{c}^*$, decreases by increasing the turbulence intensity. Specifically, increasing u'_0/U from 0.02 to 0.17 decreases $\bar{c}^*$ from 0.6 to 0.5. The following argument shows that the decreasing trend of $\bar{c}^*$ with u'_0/U is associated with counter-gradient and gradient diffusion regimes of turbulent premixed combustion. This is investigated using the Bray number, with the formulation presented in Eq. (3). As can be seen from Eqs. (2) and (3), the modification factor, α, plays a significant role in predicting the occurrence of counter-gradient or gradient diffusion in turbulent premixed flames. Veynante et al. [12] argue that α depends on the ratio of the integral length scale (Λ) to the laminar flame thickness (δ_L). Their results [12] show that changing Λ/δ_L from 4 to 40 changes α from about 0.3 to unity, following a semi-logarithmic correlation. Thus, a semi-logarithmic correlation was fitted to the results presented in [12] yielding the following expression:

$$\alpha \approx 0.74 \log \frac{\Lambda}{\delta_L} - 0.1. \tag{16}$$

In comparison to the results of Veynante et al. [12], those of Kalt and Bilger [56] show that α features an inverse linear correlation with u'_0/S_{L0}. This leads to the Bray number becoming independent the u'_0/S_{L0}, see Eq. (3). As a result, it can be inferred from the arguments of Kalt and Bilger [56] that the turbulent flux of the progress-variable is independent of u'_0/S_{L0}. This is in contrast with the results of past investigations, e.g., [9–13]. For this reason, the results presented in Veynante et al. [12], that are the values obtained from the right-hand-side of Eq. (16), were used for estimation of the modification factor.

For all the experimental conditions tested, values of N_B were estimated and presented against u'_0/S_{L0} in Fig. 15(a). Also overlaid on the figure are the data from Shepherd [16] and Tang and Chan [21]. Uncertainties associated with estimations of N_B and u'_0/S_{L0} depend on the experimental conditions tested. The error bars in the figure represent the maximum uncertainties pertaining to estimations of N_B and u'_0/S_{L0} values. As suggested by [12], $N_B = 1$ divides the diagram in Fig. 15(a) into two regions: counter-gradient and gradient diffusion regimes. The results in the figure show that all the experimental conditions associated with relatively small values of turbulence intensities, that are Flames A–F conditions, correspond to counter-gradient diffusion regime. For relatively moderate values of turbulence intensity, that are Flames G–L conditions, increasing u'_0/S_{L0} transitions the experimental conditions from regime of counter-gradient diffusion to that of gradient diffusion. The experimental conditions associated with relatively large values of turbulence intensity, Flames M–R, pertain to gradient diffusion regime.

For all experimental conditions tested, variation of the mean-progress-variable at which Σ maximizes, i.e., $\bar{c}^*$, versus N_B is presented in Fig. 15(b). Also overlaid on the figure are the experimental results of Shepherd [16] and Tang and Chan [21]. The results of the present study, in agreement with those of Shepherd [16] show that, for experimental conditions pertaining to counter-gradient diffusion regime, except Flame K condition, $\bar{c}^*$ is greater than or equal to 0.5. Also, the results of Tang and Chan [21] except the data point associated with $N_B \approx 15$ follow this trend. However, for gradient diffusion regime, $\bar{c}^*$ is smaller than or equal to 0.5. The reason for the $\bar{c}^*$ associated with Flame K condition being more than 0.5 is speculated to be linked to the experimental condition being in the transition region between counter-gradient and gradient diffusion regimes.

For counter-gradient diffusion regime, arguments provided in Shepherd [16] show that the reason for $\bar{c}^*$ being greater than 0.5 is associated with formation of cusps on the burnt side of the flame region. Indeed, our experimental results associated with relatively small and moderate values of turbulence intensities confirm the cusp formation; see for example Figs. 12(a) and (b). Increasing the turbulence intensity transitions the experimental conditions from counter-gradient to gradient diffusion regime (see, Fig. 15(a)). Arguments provided in Veynante et al. [12] show that, for gradient diffusion regime, in addition to cusp formation, the flame front features formation of small scale structures that are formed close to the reactants region. The results presented in Fig. 12(c) confirm this. The formation of small scale flame front structures close to the reactants region leads to an increase of the flame surface density at the regions associated with small values of mean-progress-variable; and, as a result, $\bar{c}^*$ transitions to values of mean-progress-variable smaller than 0.5.

Conventional algebraic models proposed in the literature, e.g., Bray–Moss–Libby model [57], assume a parabolic shape for the flame surface density profile, which features a maximum at the mean-progress-variable of $\bar{c} = 0.5$. This is in comparison with the results presented in Shepherd [16], Tang and Chan [21], as well as the results of the present study which showed $\bar{c}^*$ depends on the experimental conditions tested. Specifically, the results presented in Fig. 15(b) showed that $\bar{c}^*$ decreases by intensifying the turbulence conditions. In order to investigate the effect of u'_0/U on $\bar{c}^*$, a semi-empirical model that mimics variation of the normalized flame surface density, Σ/Σ_{max}, with $\bar{c}$ is proposed. The model is given by:

$$\frac{\Sigma}{\Sigma_{max}} = A\bar{c}^a(1-\bar{c})^b. \tag{17}$$

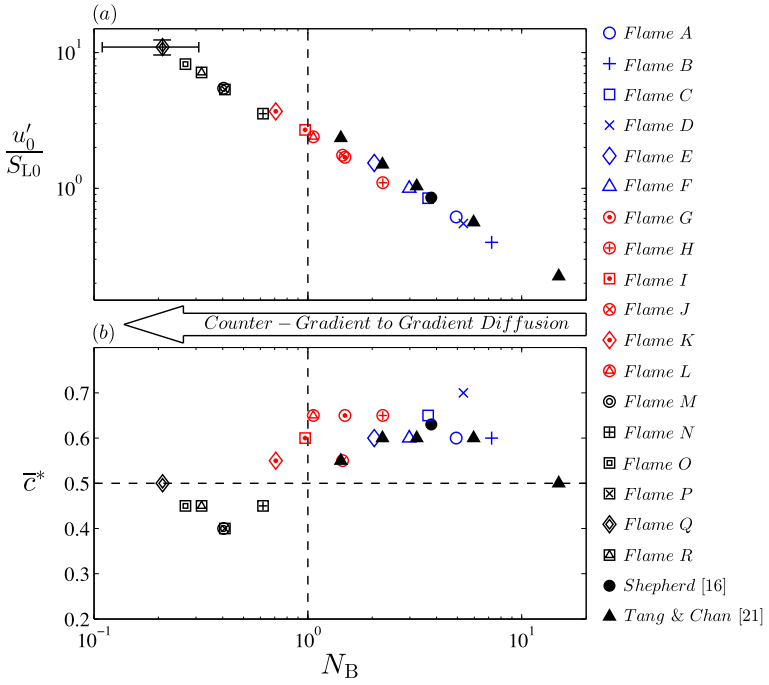

Fig. 15. (a) Regimes of counter-gradient and gradient diffusion and (b) variation of the mean-progress-variable at which flame surface density maximizes, i.e., $\bar{c}^*$, with N_B.

In Eq. (17), the multiplier A is obtained based on the condition that Σ/Σ_{max} equals to unity at its maximum. This results in: $A = (a+b)^{a+b}/(a^a b^b)$. In Eq. (17), a and b are model parameters and are obtained by fitting the equation to the experimental results using the least-square technique. Analysis of the results show that, for all experimental conditions tested, $b \approx 0.7$. Values of a are listed in Table 1. Also presented in the table are the values of Σ_{max}. The results show that both a and Σ_{max} are significantly dependent on the turbulence intensity. Specifically, increasing u'_0/U decrease both a and Σ_{max}. Using the formulation proposed in Eq. (17) along with the maximum flame surface density data, the predictions of the model for experimental conditions of Flames E, K, and Q were obtained. The profiles are presented by the dashed lines in Fig. 14(c). The model predictions show reasonable agreement with the experimental results. This suggests that the formulation proposed in Eq. (17) can be potentially utilized in numerical simulation studies of turbulent premixed V-shaped flames.

3.2.3. Averaged local consumption speed and turbulent burning velocity

Figure 16 represents a curvilinear coordinate system usually utilized for studying the local consumption speed in turbulent premixed flames, see for example Sattler et al. [58]. In the figure, ξ is a curved axis overlaid on the contour of $\bar{c} = 0.5$. η-axes are normal to the mean-progress-variable contours with their origins positioned on the ξ-axis. It can be shown that the local consumption speed, with the formulation provided in Eq. (6), depends on the selection of the η-axis. For this reason, an averaged local consumption speed was estimated in the present study. This averaging is performed along the axis of ξ, and the corresponding mathematical operation is denoted by a double-bar sign. The averaged local consumption speed is given by:

$$\overline{\overline{S_{LC}}} = \frac{\int_0^l S_{LC}\,d\xi}{\int_0^l d\xi}, \tag{18}$$

where l is the length of the contour pertaining to $\bar{c} = 0.5$. It is shown in Appendix A that the formulation provided in Eq. (18) can be simplified to the following equation:

$$\overline{\overline{S_{LC}}} \approx S_{L0}\overline{\overline{\delta_t \cos(\psi)}} \int_0^1 \Sigma\,d\bar{c}. \tag{19}$$

Eq. (19) indicates that the averaged local consumption speed ($\overline{\overline{S_{LC}}}$) is approximately equal to the multiplication of unstretched laminar flame speed, a spatially-averaged flame brush thickness projected in the direction normal to the counter of $\bar{c} = 0.5$, and integration of the flame surface density with respect to the mean-progress-variable. This result is similar to that presented in Shepherd [16].

The angle ψ was estimated from mean-progress-variable contours; and variation of $\delta_t \cos(\psi)$ versus ξ is presented in Fig. 17. The results are shown for a fixed value of mean bulk flow velocity ($U = 8.3$ m/s) and for a fixed value of fuel–air equivalence ratio ($\phi = 0.6$). As can be seen from the results in the figure, for a given ξ, increasing the turbulence intensity increases $\delta_t \cos(\psi)$. This means that, increasing the turbulence intensity increases $\overline{\delta_t \cos(\psi)}$. On the other hand, results presented in Fig. 14(c) showed

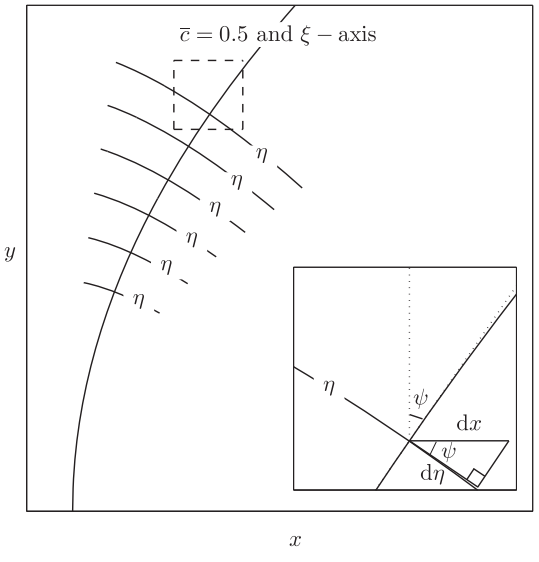

Fig. 16. Curvilinear coordinate system.

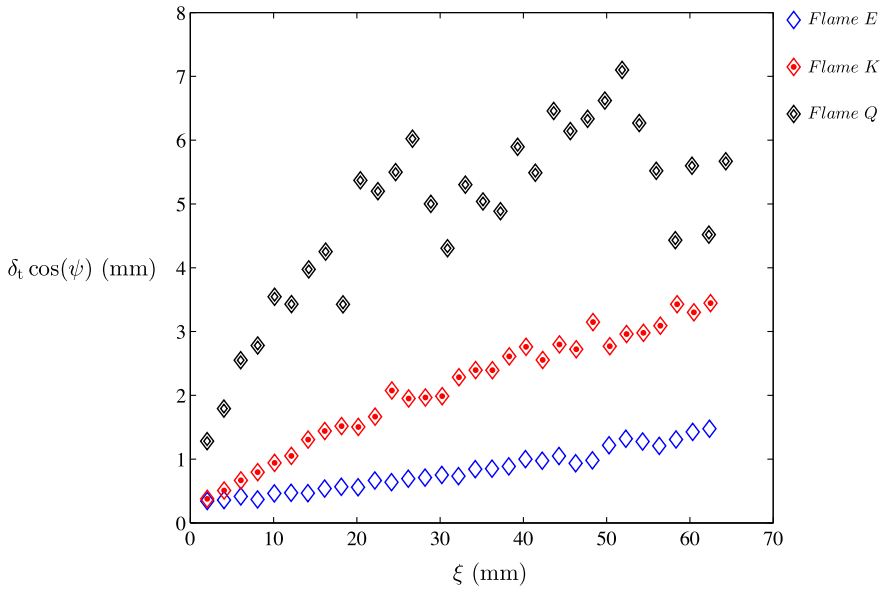

Fig. 17. Variation of the flame brush thickness in the direction normal to $\bar{c} = 0.5$ along the ξ-axis. For the results presented in the figure, the mean bulk flow velocity and the fuel–air equivalence ratio are fixed at 8.3 m/s and 0.6, respectively. The turbulence intensities associated with Flames E, K, and Q are 0.02, 0.06, and 0.17, respectively.

that increasing the turbulence intensity decreases $\int_0^1 \Sigma \, d\bar{c}$. Based on Eq. (19), this argument suggests that the trend associated with the effect of turbulence intensity on the averaged local consumption speed is not known a priori.

Using the flame brush thickness data, the angle between tangent to the contour of $\bar{c} = 0.5$ and the vertical axis, and the flame surface density data, the averaged local consumption speed was estimated using Eq. (19). Shepherd [16] and Sattler et al. [58] estimated the local consumption speed at several vertical distances from the flame-holder. For relatively moderate values of the turbulence intensity, which is the case for the studies of [16,58], it can be shown that variation of ξ with y represents a line. This means that, the averaged local consumption speed can be estimated from:

$$\overline{\overline{S_{LC}}} = \frac{\int_0^l S_{LC} \, d\xi}{\int_0^l d\xi} \approx \frac{\int_0^{y_{max}} S_{LC} \, dy}{\int_0^{y_{max}} dy}, \tag{20}$$

where y_{max} is the maximum vertical distance from the flame-holder. The implication of the approximation in Eq. (20) is that, for relatively moderate values of turbulence intensity, the averaged local consumption speed can be estimated by averaging the local consumption speed data along the vertical axis. The estimated values of $\overline{\overline{S_{LC}}}$ are presented in Fig. 18. The averaged local consumption speed associated with the studies of [16,58] were estimated by finding the mean of the reported local consumption speed values at several vertical distances from the flame-holder; and were overlaid in Fig. 18. The results are normalized by the unstretched laminar flame speed and are presented as a function of u'_0/S_{L0}. In past experimental investigations, see [6,59], variation of the local consumption speed has been mainly presented as a function of u'_0/S_{L0}. For this reason the results in Fig. 18 are presented against the u'_0/S_{L0}. Also, overlaid on the figure are the results of Shepherd [16] and Sattler et al. [58]. The results associated with small values of u'_0/U

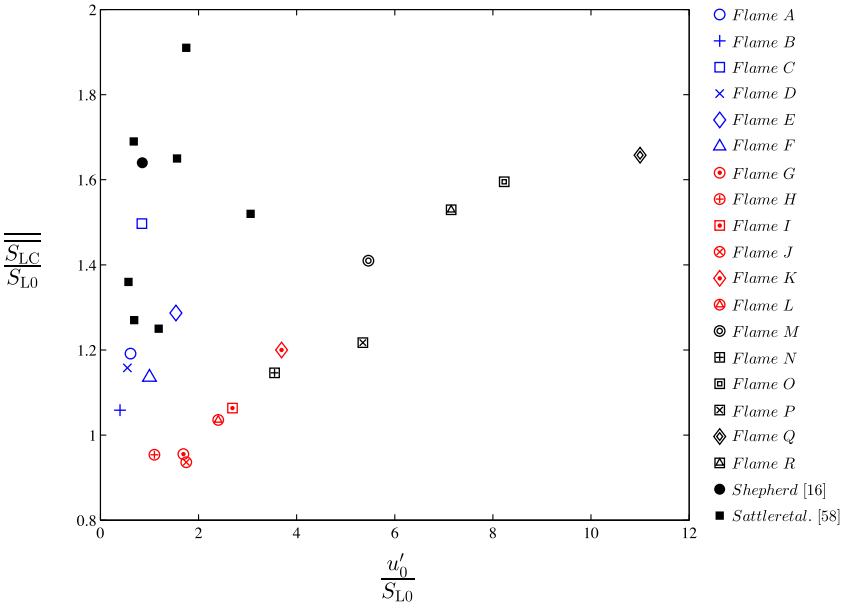

Fig. 18. Spatially-averaged local consumption speed normalized by the unstretched laminar flame speed.

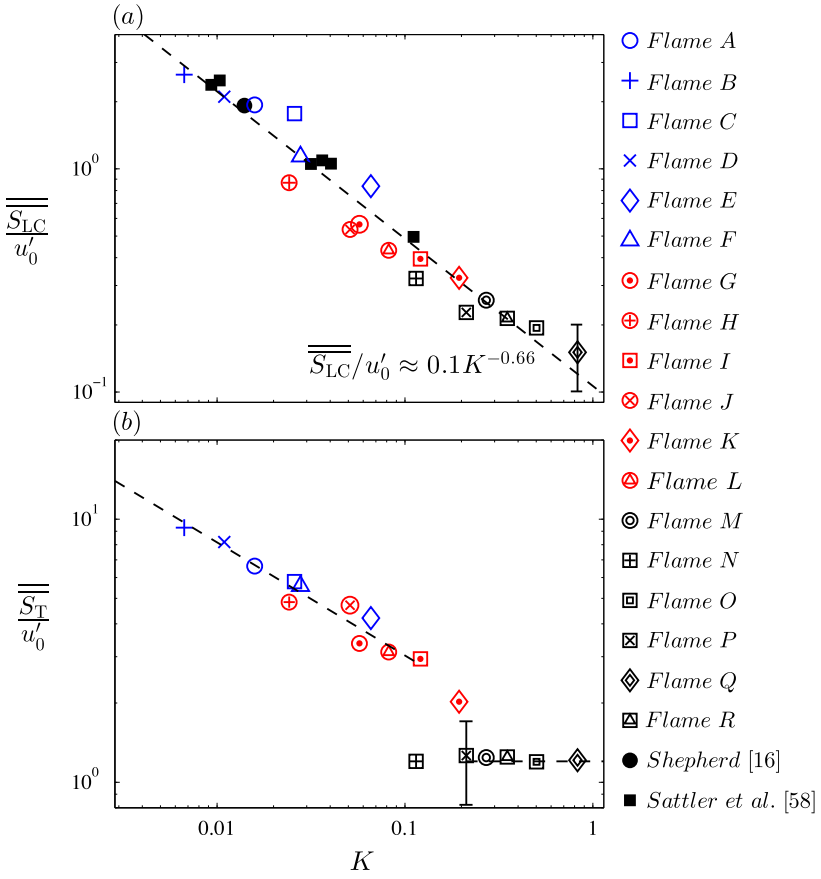

Fig. 19. (a) Normalized spatially-averaged local consumption speed and (b) normalized spatially-averaged turbulent burning velocity.

and those associated with Shepherd [16] and Sattler et al. [58] show significant scatter. However, for relatively moderate and large values of u'_0/U, that are conditions of Flames G–R, the results show that increasing u'_0/S_{L0} increases the normalized and averaged local consumption speed. This is in agreement with the results presented in [6,8] for turbulent premixed flames.

Figure 18 shows that presentation of the results as a function of u'_0/S_{L0} do not lead to collapse of the averaged local consumption speed data. It is previously shown in past studies, e.g., Bradley et al. [28], that the Karlovitz stretch factor can potentially lead to collapse of the data. Thus, the averaged local consumption speed normalized by the RMS of the streamwise velocity is presented as a function of the Karlovitz stretch factor in Fig. 19(a). In past investigations, e.g., [28], multiplication of the Karlovitz stretch factor and the Lewis number has been utilized. However, since the Lewis number is constant in the present study, the results are presented only as a function of the Karlovitz stretch factor. The uncertainty associated with the averaged local consumption speed depends on the experimental conditions tested. The maximum uncertainty of $\overline{\overline{S_{LC}}}/u'$ pertains to the experimental condition of Flame Q, and is accommodated by the size of the error bar in Fig. 19(a). Also, overlaid on the figure are the results of Shepherd [16] and Sattler et al. [58]. Comparison of the results of the present study and those of [16,58] shows reasonable agreement. The results of the present study as well as those of [16,58] show that the normalized averaged local consumption speed decreases with increasing K. Least-square fit to the results presented in Fig. 19(a) shows that $\overline{\overline{S_{LC}}}/u'$ follows a power-law relation with K given by the following formulation:

$$\frac{\overline{\overline{S_{LC}}}}{u'_0} \approx 0.1K^{-0.66}. \tag{21}$$

The power-law correlation between the Karlovitz stretch factor and $\overline{\overline{S_{LC}}}/u'_0$ is due to the scaling utilized in Eq. (21) and is in agreement with past studies, see for example Bradley et al. [28]. Utilizing the definition of the Karlovitz stretch factor, i.e., Eq. (10), along with the definition of the laminar flame thickness provided in previous section, it can be shown that Eq. (21) reduces to:

$$\frac{\overline{\overline{S_{LC}}}}{S_{L0}} \approx 0.38\left(\frac{\Lambda}{\delta_L}\right)^{0.33}. \tag{22}$$

Results presented in Fig. 4 shows that the normalized integral length scale (Λ_0/δ_L) varies between 15 and 60. Thus, Eq. (22) suggests that the normalized and spatially-averaged local consumption speed varies between unity and 1.5, which is in agreement with the results presented in Fig. 18.

Averaged turbulent burning velocity ($\overline{\overline{S_T}}$) was estimated for all the experimental conditions tested using the following equation:

$$\overline{\overline{S_T}} = \frac{\int_0^l S_T \mathrm{d}\xi}{\int_0^l \mathrm{d}\xi}. \tag{23}$$

The upper bound of integrals in Eq. (23), i.e., l, depends on the vertical extent of the domain of investigation (y_{max}). Details associated with the effect of y_{max} on $\overline{\overline{S_T}}$ are discussed in Appendix B. In addition to the vertical extent of the domain of investigation, the horizontal extent can potentially affect the values of the spatially-averaged turbulent burning velocity due to possible existence of flame surfaces outside of the domain of investigation. In the present study, however, the domain is selected large enough such that the flame surfaces do not exist outside of the domain of investigation. This is because the flame surfaces are bound between the jet shear layer, and these shear layers are included in the domain of investigation.

Values of the spatially-averaged turbulent burning velocity normalized by u'_0 are presented in Fig. 19(b). The results are plotted against K. The error bar in the figure pertains to the maximum uncertainty in estimation of $\overline{\overline{S_T}}/u'_0$. Two asymptotic trends can be identified in Fig. 19(b). The first trend pertains to $K \lesssim 0.1$, which is associated with relatively small and moderate values of turbulence intensities. The second trend pertains to $K \gtrsim 0.2$, which consists of the experimental conditions associated with relatively large values of turbulence intensities. For $K \lesssim 0.1$, results of the present study show that increasing K decreases $\overline{\overline{S_T}}/u'_0$. In comparison to the results associated with $K \lesssim 0.1$, those pertaining to $K \gtrsim 0.2$ show that the normalized turbulent burning velocity is approximately constant ($\overline{\overline{S_T}}/u'_0 \approx 1.2$). This means that, for relatively large values of turbulence intensity ($u'_0/U \approx 0.17$), the turbulent burning velocity is independent of stretching of the flame front and increases almost linearly with increasing RMS of reactants velocity.

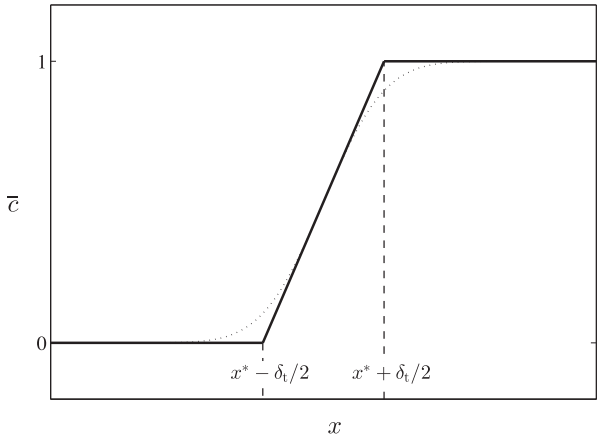

Fig. 20. Variation of the mean-progress-variable with the transverse direction. The solid line corresponds to the correlation presented in Eq. (A3). The dotted-line pertains to an error-function type variation for the mean-progress-variable.

4. Concluding remarks

Flame surface density, local consumption speed, and turbulent burning velocity of turbulent premixed V-shaped flames were investigated experimentally. The experiments were performed for three mean bulk flow velocities of $U = 4.0$, 6.2, and 8.3 m/s, along with two fuel–air equivalence ratios of $\phi = 0.6$ and 0.7. For each mean bulk flow velocity and fuel–air equivalence ratio, relatively small ($u'_0/U \approx 0.02$), moderate ($u'_0/U \approx 0.06$), and large ($u'_0/U \approx 0.17$) values of turbulence intensities were tested.

The results show that the mean-progress-variable at which the flame surface density maximizes ($\bar{c}^*$) is significantly dependent on the turbulence intensity tested. Specifically, for relatively small and moderate values of turbulence intensities, the flame surface densities maximize at mean-progress-variables greater than 0.5. However, increasing u'_0/U decreases $\bar{c}^*$ to values smaller than 0.5. This was linked to change of the experimental conditions from counter-gradient to gradient diffusion regime of turbulent premixed combustion. A semi-empirical correlation was proposed to model this characteristic of the flame surface density.

Values of both spatially-averaged local consumption speed and turbulent burning velocity were estimated. The results pertaining to the spatially-averaged local consumption speed show that it varies between the unstretched laminar flame speed and 1.5 times the unstretched laminar flame speed. The results pertaining to the spatially-averaged normalized turbulent burning velocity show that this parameter depends on the Karlovitz stretch factor. For $K \lesssim 0.1$, the normalized turbulent burning velocity decreases with increasing K. For relatively large values of the Karlovitz stretch factor, that are mainly conditions with relatively large values of turbulence intensity, the results show that the spatially-averaged turbulent burning velocity is almost proportional to the RMS of the streamwise velocity.

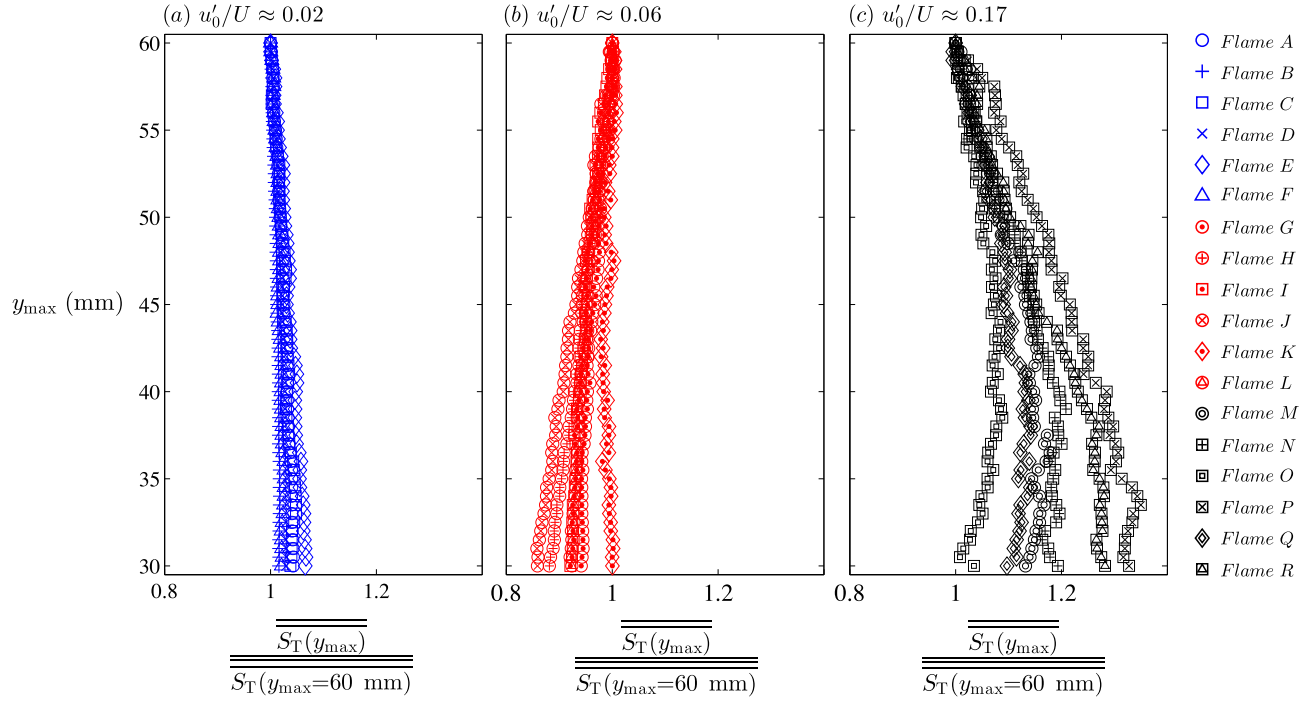

Fig. 21. Effect of the vertical extent of the domain of investigation on the spatially-averaged turbulent burning velocity. (a), (b), and (c) correspond to relatively small, moderate, and large values of the turbulence intensity.

Acknowledgment

The authors are grateful for financial support from the Natural Sciences and Engineering Research Council (NSERC) of Canada.

Appendix A. Derivation of a simplified formulation for the averaged local consumption speed

Eq. (19) was used for estimation of the averaged local consumption speed ($\overline{\overline{S_{LC}}}$). The formulation for the local consumption speed (S_{LC}) is given by Eq. (6). Using trigonometric arguments (see Fig. 16), it can be shown that:

$$d\eta \approx dx\cos(\psi). \tag{A1}$$

Thus, Eq. (6) can be simplified to:

$$S_{LC} \approx S_{L0} I_0 \int_{-\infty}^{+\infty} \Sigma dx \cos(\psi). \tag{A2}$$

The mean-progress-variable ($\bar{c}$) features an error-function type correlation with x, see for example Kheirkhah and Gülder [32]. In the present study, this correlation is simplified and is given by:

$$\bar{c} = \begin{cases} 0, & x < x^* - \delta_t/2, \\ (x - x^*)/\delta_t + 1/2, & x^* - \delta_t/2 \leqslant x \leqslant x^* + \delta_t/2, \\ 1, & x > x^* + \delta_t/2, \end{cases} \tag{A3}$$

where x^* is the transverse position of $\bar{c} = 0.5$ at a given height from the flame-holder. The simplified correlation between $\bar{c}$ and x is presented in Fig. 20. Also overlaid on the figure is an error-function correlation between $\bar{c}$ and x. The results in the figure show that the formulation provided in Eq. (A3) provides a reasonable first order approximation for the correlation between $\bar{c}$ and x.

Using the correlations in Eq. (A3), Eq. (A2) was simplified to:

$$S_{LC} \approx S_{L0} I_0 \int_0^1 \Sigma \delta_t \cos(\psi) d\bar{c}. \tag{A4}$$

The integral in Eq. (A4) pertains to a fixed η-axis. Thus, for a given η-axis, $\delta_t \cos(\psi)$ is fixed and independent of the mean-progress-variable. Also, for lean methane–air premixed flames, which pertain to the experimental conditions of the present study, the stretch factor (I_0) is approximately unity [6]. Thus, combining Eqs. (A4) and (18) results in:

$$\overline{\overline{S_{LC}}} \approx S_{L0} \int_0^1 \Sigma d\bar{c} \frac{\int_0^l \delta_t \cos(\psi) d\xi}{\int_0^l d\xi} = S_{L0} \overline{\overline{\delta_t \cos(\psi)}} \int_0^1 \Sigma d\bar{c}. \tag{A5}$$

Appendix B. Effect of vertical extent of the domain of investigation on turbulent burning velocity

Eq. (23) shows that the spatially-averaged burning velocity depends on l, which is the length of the contour pertaining to $\bar{c} = 0.5$. For each experimental condition tested, l varies by changing the vertical extent of the domain of investigation (y_{max}). Figure 21 represents the effect of y_{max} on the spatially-averaged turbulent burning velocity. Figures 21(a), (b), and (c) correspond to turbulence intensities of $u_0'/U \approx 0.02$, 0.06, and 0.17, respectively. For each experimental condition tested, the results are normalized by the pertaining value of the spatially-averaged turbulent burning velocity estimated at $y_{max} = 60$ mm. The results in Fig. 21 show that dependence of the spatially-averaged turbulent burning velocity becomes more pronounced with increasing the turbulence intensity. The maximum variation pertains to Flame P condition which is about 35%. Uncertainty analysis shows that, for our experiments, error in estimation of $\overline{\overline{S_T}}$ caused by the variation in the vertical extent of the domain of investigation is significantly larger than other sources of error. The maximum uncertainty pertaining to estimation of the spatially averaged turbulent burning velocity is presented by the size of the error bar in Fig. 19(b).

References

[1] N. Peters, Turbulent Combustion, first ed., Cambridge University Press, 2000.
[2] I. Glassman, R.A. Yetter, Combustion, fourth ed., Elsevier Inc., 2008.
[3] R.V. Kuznetsov, V.A. Sabel'nikov, P.A. Libby, Turbulence and Combustion, first ed., Hemisphere Publishing Corporation, 1990.
[4] P. Koutmos, J.J. McGuirk, Exp. Fluids 7 (1989) 344–354.
[5] P. Clavin, Prog. Energy Combust. Sci. 11 (1985) 1–59.
[6] J.F. Driscoll, Prog. Energy Combust. Sci. 34 (2008) 91–134.
[7] S.J. Shanbhogue, S. Husain, T. Lieuwen, Prog. Energy Combust. Sci. 35 (2009) 98–120.
[8] A.N. Lipatnikov, J. Chomiak, Combust. Sci. Technol. 165 (2001) 175–195.
[9] J.B. Moss, Combust. Sci. Technol. 22 (1980) 119–129.
[10] P.A.M. Kalt, J.H. Frank, R.W. Bilger, Proc. Combust. Inst. (1998) 751–758.
[11] J.H. Frank, P.A.M. Kalt, R.W. Bilger, Combust. Flame 116 (1999) 220–232.
[12] D. Veynante, A. Trouvé, K.N.C. Bray, T. Mantel, J. Fluid Mech. 332 (1997) 263–293.
[13] N. Swaminathan, R.W. Bilger, G.R. Ruetsch, Combust. Sci. Technol. 128 (1997) 73–97.
[14] K.N.C. Bray, P.A. Libby, J.B. Moss, Combust. Flame 61 (1985) 87–102.
[15] S. Pfadler, A. Leipertz, F. Dinkelacker, J. Wäsle, A. Winkler, T. Sattelmayer, Proc. Combust. Inst. 31 (2007) 1337–1344.
[16] I.G. Shepherd, Proc. Combust. Inst. 26 (1996) 373–379.
[17] H. Guo, B. Tayebi, C. Galizzi, D. Escudié, Int. J. Hydrogen Energy 35 (2010) 11342–11348.
[18] J.B. Bell, M.S. Day, I.G. Shepherd, M.R. Johnson, R.K. Cheng, J.F. Grcar, V.E. Beckner, M.J. Lijewski, Proc. Natl. Acad. Sci. USA 102 (29) (2005) 10006–10011.
[19] D. Veynante, J.M. Duclos, J. Piana, Proc. Combust. Inst. 25 (1994) 1249–1256.
[20] J.S.L. Lam, C.K. Chan, L. Talbot, I.G. Shepherd, Combust. Theor. Model. 7 (2003) 1–28.
[21] B.H.Y. Tang, C.K. Chan, Combust. Flame 147 (2006) 49–66.
[22] F.C. Gouldin, P.C. Miles, Combust. Flame 100 (1995) 202–210.
[23] C. Ghenai, F.C. Gouldin, I. Gökalp, Proc. Combust. Inst. (1998) 979–987.
[24] D.C. Bingham, F.C. Gouldin, D.A. Knaus, Proc. Combust. Inst. (1998) 77–84.
[25] D. Durox, S. Ducruix, S. Candel, Combust. Flame 125 (2001) 982–1000.
[26] L.K. Tseng, M.A. Ismail, G.M. Faeth, Combust. Flame 95 (1993) 410–426.
[27] C.J. Sun, C.J. Sung, L. He, C.K. Law, Combust. Flame 118 (1999) 108–128.
[28] D. Bradley, A.K.C. Lau, M. Lawes, Philos. Trans. Roy. Soc. London A 338 (1992) 359–387.
[29] A.C. Eckbreth, Laser Diagnostics for Combustion Temperature and Species, second ed., Overseas Publishers Association, 1996.
[30] N. Peters, Proc. Combust. Inst. 21 (1986) 1231–1250.
[31] P. Goix, P. Paranthoen, M. Trinite, Combust. Flame 81 (1990) 229–241.
[32] S. Kheirkhah, Ö.L. Gülder, Phys. Fluids 25 (2013) 055107.
[33] S. Kheirkhah, Ö.L. Gülder, Combust. Flame 161 (2014) 2614–2626.
[34] S. Kheirkhah, Ö.L. Gülder, Flow, Turbul. Combust. 93 (2014) 439–459.
[35] S.A. Filatyev, J.F. Driscoll, C.D. Carter, J.M. Donbar, Combust. Flame 141 (2005) 1–21.
[36] T. Lachaux, F. Halter, C. Chauveau, I. Gökalp, I.G. Shepherd, Proc. Combust. Inst. 30 (2005) 819–826.
[37] G. Yu, C.K. Law, C.K. Wu, Combust. Flame 63 (1986) 339–347.
[38] R.G. Abdel-Gayed, D. Bradley, M. Lawes, Proc. Roy. Soc. London A 414 (1987) 389–413.
[39] Y.-C. Chen, N. Peters, G.A. Schneemann, N. Wruck, U. Renz, M.S. Mansour, Combust. Flame 107 (1996) 223–244.
[40] Y.-C. Chen, R.W. Bilger, Exp. Therm. Fluid Sci. 27 (2003) 619–627.
[41] Y.-C. Chen, R. Bilger, Combust. Sci. Technol. 167 (2001) 131–167.
[42] H. Makita, Fluid Dyn. Res. 8 (1991) 53–64.
[43] A.A. Verbeek, R.C. Pos, G.G.M. Stofels, B.J. Geurts, T.H. van der Meer, Exp. Fluids 54 (2013) 1594.
[44] N. Mazellier, L. Danaila, B. Renou, J. Turbul. 11 (43) (2010) 1–30.
[45] N. Mazellier, J.C. Vassilicos, Phys. Fluids 22 (2010) 075101.
[46] R. Gomes-Fernandes, B. Ganapathisubramani, J.C. Vassilicos, J. Fluid Mech. 711 (2012) 306–336.
[47] L. BogusŁawski, C.O. Popiel, J. Fluid Mech. 90 (1979) 531–539.
[48] T.H. Weisgraber, D. Liepmann, Exp. Fluids 24 (1998) 210–224.
[49] G. Xu, R.A. Antonia, Exp. Fluids 33 (2002) 677–683.
[50] S.J. Kwon, I.W. Seo, Exp. Fluids 38 (2005) 801–812.
[51] S. Daniele, J. Mantzaras, P. Jansohn, A. Denisov, K. Boulouchos, J. Fluid Mech. 724 (2013) 36–68.
[52] R.A. Antonia, L.W.B. Browne, S. Rajagopalan, A.J. Chambers, J. Fluid Mech. 134 (1983) 49–66.
[53] M.M. Zdravkovich, Flow Around Circular Cylinders: Fundamentals, vol. 1, Oxford University Press, 1997.
[54] S. Pfadler, M. Löffler, F. Dinkelacker, A. Leipertz, Exp. Fluids 39 (2005) 375–384.
[55] M. Namazian, I.G. Shepherd, L. Talbot, Combust. Flame 64 (1986) 299–308.
[56] P.A.M. Kalt, R.W. Bilger, Combust. Sci. Technol. 153 (2000) 213–221.
[57] K.N.C. Bray, N. Peters, Turbulent Reacting Flows, Academic Press, London, 1994.
[58] S.S. Sattler, D.A. Knaus, F.C. Gouldin, Proc. Combust. Inst. 29 (2002) 1785–1792.
[59] A.N. Lipatnikov, J. Chomiak, Prog. Energy Combust. Sci. 28 (2002) 1–74.